Extrinsic and Intrinsic Symmetry Breaking for Field-Free Spin-Orbit Torque Switching

Mengfan Zhao(赵梦凡)[1,#], Zhicheng Wang(王志成)[2,#], Kun Ye(叶坤)[1], Fang Zhang(张芳)[1,*], Zhiyan Jia(贾志研)[1,*], Yong Jiang(姜勇)[1]

[1]Institute of Quantum Materials and Devices, State Key Laboratory of Advanced Separation Membrane Materials, School of Materials Science and Engineering, Tiangong University, Tianjin, 300387, China

[2]Shanxi Key Laboratory of Magnetic and Electric Functional Materials and Applications, College of Material Science and Engineering, Taiyuan University of Science and Technology, Taiyuan, 030024, China

[*]Corresponding author. E-mail: jiazhiyan@tiangong.edu.cn (Z. Jia); zhangf@tiangong.edu.vn (F. Zhang)

[#]These authors contributed equally to this work.

Abstract

Spin-orbit torque (SOT) enables efficient manipulation of magnetization. Owing to its advantages of high speed, superior endurance, and low power consumption, SOT is attractive for non-volatile memory and logic devices, and emerges as a core writing mechanism for next-generation magnetic random-access memory. In conventional heavy-metal/ferromagnet heterostructures, the spin Hall effect generates only in-plane spin polarization. Consequently, deterministic SOT switching of perpendicular magnetization relies on an external magnetic field to break symmetry, which imposes a critical limitation on high-density device integration. Over the past several decades, field-free switching has been realized through various strategies, such as wedge-shaped films, composition grading, exchange bias, and canted magnetic moments. However, these approaches typically suffer from slow switching speed, high power

consumption, and complex fabrication. Low-symmetry van der Waals (vdW) topological semimetals—including WTe_2, $TaIrTe_4$, and $NbIrTe_4$—offer a fundamentally new route for field-free switching. Originating from intrinsic crystal symmetry breaking, their unconventional spin polarization drives robust field-free SOT switching without relying on an external magnetic field. This review systematically summarizes the evolution of field-free SOT switching. We analyze the intrinsic bottlenecks of conventional SOT architectures, then elaborate various categories of symmetry-breaking strategies toward field-free switching, and highlight the unique merits of low-symmetry vdW spin-source materials. In addition, we discuss functional implementations of all-vdW SOT spintronic devices for in-memory logic, nonvolatile magnetic memory, and neuromorphic computing, and conclude by outlining unresolved challenges and prospective research pathways.

Keywords: Spin-orbit torque, field-free, out-of-plane spin polarization, van der Waals

PACS: 72.25.Mk, 75.78.Jp, 73.21.Cd, 85.75.Hh

1. Introduction

Spin-transfer torque (STT) manipulates magnetization via spin-polarized charge current passing through magnetic tunnel junctions, which has laid the technical foundation for commercial magnetoresistive random access memory (MRAM) chips.[1-3] Nevertheless, STT suffers from intrinsic drawbacks including shared read-write current paths, limited endurance, and risk of tunnel barrier breakdown under large write currents.[4, 5] Compared with STT, spin-orbit torque (SOT) features separated read and write paths.[6-9] Benefiting from faster magnetization switching, better cycling endurance and lower write energy consumption, SOT has attracted extensive research interest in spintronics.[8, 10-15] Among various SOT devices, those with perpendicular magnetic anisotropy (PMA) stand out for high-density memory applications, as they exhibit enhanced thermal stability and better scalability at nanoscale

dimensions.[8, 15]

Even with these merits, conventional heavy-metal/ferromagnet (HM/FM) structures[11, 16-22] are bounded by a fundamental symmetry-imposed constraint. In such systems, the spin Hall effect (SHE) generates in-plane spin polarization that is always points perpendicular to the charge current.[12, 19, 22-24] For perpendicular magnetic moments, the damping-like torque from in-plane spin polarization can only tilt the magnetic moments away from their easy axis. It cannot lift the energy degeneracy between the two stable magnetization states, namely “up” and “down”.[25, 26] Consequently, an in-plane auxiliary magnetic field is indispensable for deterministic SOT switching. Reliance on an external magnetic field raises device power consumption and complicates circuit design, while hindering the high-density integration of memory cells.[27, 28] Field-free SOT switching has therefore become a central research goal in this field.

To circumvent the mandatory external field requirement, a series of extrinsic symmetry-engineering approaches have been explored to lift magnetic-state degeneracy via artificially introduced structural or magnetic asymmetry (Fig. 1 left semicircle), such as wedge-shaped layers,[29-31] composition gradients,[32] exchange bias,[33-35] and tilted magnetic anisotropy.[36-38] While these strategies prove field-free switching is possible. However, they demand extra fabrication steps, restrict the choice of materials, and often compromise switching speed, thermal stability, or wafer-scale uniformity.[30, 32-35, 39-43] As spintronic devices advance toward ultra-fast and ultra-high-density designs, researchers need to exploit intrinsic material properties. The ideal solution is to generate out-of-plane (OOP) spin polarization by breaking the inherent crystal symmetry of spin-source materials.[44-49] This approach fundamentally removes the need for external magnetic fields.

The discovery of low-symmetry van der Waals (vdW) materials offers a new route to realize field-free SOT switching. Prototypical low-symmetry crystals such as WTe_2,[47, 48, 50-58] $TaIrTe_4$,[45, 46, 59-61] and $NbIrTe_4$[44, 62] produce OOP spin polarization when current flows along crystal directions with broken symmetry (Fig. 1 right semicircle). The resulting unconventional damping-like torque acts directly on the perpendicular magnetic moment of an adjacent ferromagnet. Deterministic SOT switching can thus be realized without external magnetic

fields or artificial structural modification.[44-46, 48] When these low-symmetry spin-sources materials stack with ferromagnets including Fe_3GeTe_2 (FGeT)[63-65] and Fe_3GaTe_2 (FGaT),[66-69] all two-dimensional (2D) vdW SOT heterostructures form.[70] These heterostructures feature atomically sharp interfaces, strong spin-orbit coupling (SOC), and gate-voltage tunability.[58, 71-74] Thanks to these unique advantages, SOT devices built on this planform show strong potential for advanced computing architectures, including high-speed cache, in-memory computing, and non-volatile logic.[6, 15, 70, 75-79]

Building upon this progressive technical evolution from extrinsic artificial symmetry modification toward intrinsic crystal-symmetry breaking, this review systematically surveys the physical origin of OOP spin-polarization generation. We analyze the intrinsic limitations of conventional extrinsic field-free schemes, elaborate unconventional SOT physics hosted by low-symmetry vdW spin-source materials, and summarize recent advances in functional all-vdW spintronic integrated devices.

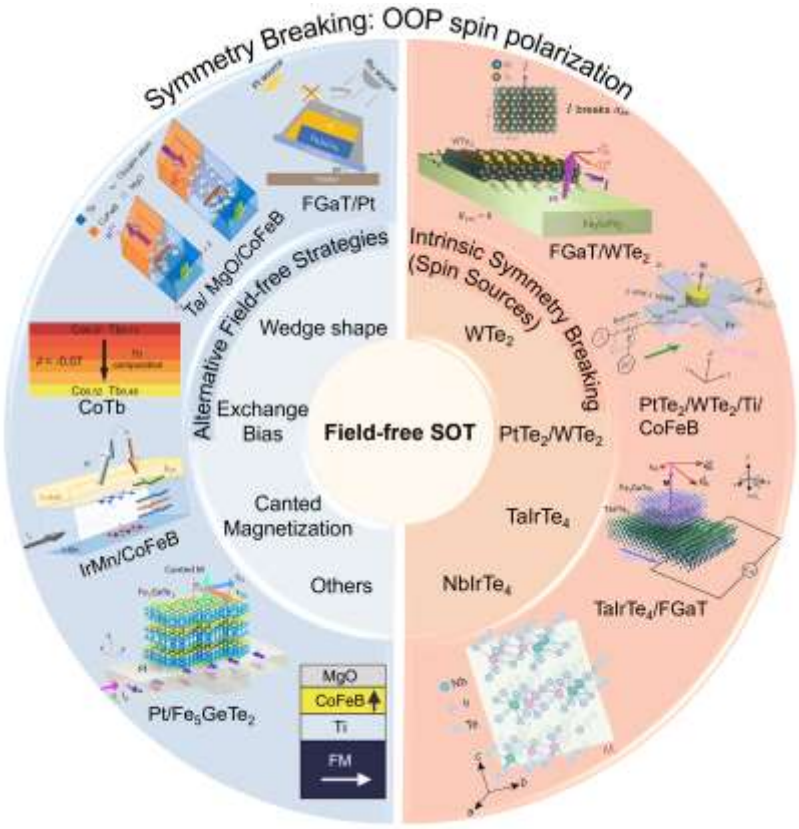


Fig. 1. Core strategies for field-free SOT switching of perpendicular magnetization. This circular roadmap classifies technical routes toward field-free deterministic magnetization reversal and categorizes them into

two distinct symmetry-breaking paradigms. The left semicircle (light blue) summarizes strategy based on artificial extrinsic symmetry breaking. Effective built-in fields are introduced via compositional, structural, or magnetic modifications to substitute required in-plane assisting field. Representative routes cover exchange bias, wedge-shaped asymmetric films, canted magnetic moments, and other schemes, alongside typical device structures including IrMn/CoFeB,[33] composition-graded CoTb,[32] tilted Pt/FGaT,[40] FM/Ti/CoFeB/MgO[39] and Pt/Fe_5GeTe_2.[36] The right semicircle (warm orange) presents the intrinsic symmetry breaking paradigm based on low-symmetry vdW spin-source materials. Native mirror symmetry breaking along specific crystal directions directly generates OOP spin polarization, which supports field-free SOT switching without additional structural modifications. Key topological semimetal spin-source materials including WTe_2, $TaIrTe_4$, and $NbIrTe_4$ are presented, along with their functional heterostructures (e.g., WTe_2/FGaT,[48] $TaIrTe_4$/FGaT,[45] $PtTe_2$/WTe_2/Ti/CoFeB[78]) and corresponding OOP SOT generation mechanisms. SOT vector distributions and device stacking configurations are annotated across both regions. All above engineering strategies converge to a unified physical target: deterministic perpendicular magnetization switching driven by spin–orbit coupling without external magnetic bias. Reprinted with permission from Ref. [39]. Copyright 2018 Springer Nature. Reprinted with permission from Ref. [30]. Copyright 2019 American Chemical Society. Reprinted with permission from Ref. [33]. Copyright 2016 Springer Nature. Reprinted with permission from Ref. [32] under the terms of the CC-BY 4.0 license. Reprinted with permission from Ref. [40] under the terms of the CC-BY 4.0 license. Reprinted with permission from Ref. [36]. Copyright 2025 American Chemical Society. Reprinted with permission from Ref. [48] under the terms of the CC-BY 4.0 license. Reprinted with permission from Ref. [78]. Copyright 2025 Wiley-VCH GmbH. Reprinted with permission from Ref. [45] under the terms of the CC-BY 4.0 license. Reprinted with permission from Ref. [44]. Copyright 2026 American Chemical Society.

2. Field-dependent SOT switching

In conventional HM/FM devices, the spin polarization is strictly confined in the film plane. Therefore, the external in-plane field is indispensable to break the mirror asymmetry and realize the deterministic SOT switching.[80-88] Even in a centrally symmetric bulk ferromagnets, such as $L1_0$ FePt in Fig. 2(a), switching hysteresis vanishes under zero in-plane field, and reversing H_x flips the magnetization switching polarity, which verifies the symmetry-breaking function of external magnetic fields.[89] In vdW materials, ferromagnets FGeT and FGaT possess strong PMA.[63, 64, 66, 69, 90-92] By combining the commonly used spin-source material Pt with FGeT, temperature-dependent switching phase diagram is established for Pt/FGeT vdW heavy-metal heterostructure (Fig. 2(b)). Under the in-plane magnetic field, the critical switching current decreases with the increase of temperature, which is attributed to the weakening of PMA and coercivity at high temperature.[86] Moreover, Pt/FGaT device enables

SOT-driven perpendicular magnetization switching up to 300 K, but deterministic reversal still relies on an external in-plane auxiliary magnetic field (Fig. 2(c)).[93]

Topological insulators (TI) exploit spin-momentum-locked topological surface states (TSS) for efficient charge-spin conversion, yet their heterostructures with vdW ferromagnets still require an in-plane field for deterministic SOT switching. In $Cr_2Ge_2Te_6$ (CGT)/$(Bi, Sb)_2Te_3$ (BST) device, SOT switching is realized under a fixed 0.1 T in-plane field (Fig. 2(d)).[94] Fermi level (E_F) engineering via alloying or gating optimizes the field-dependent SOT response. Fig. 2(e) illustrates that for the V-doped $(Bi, Sb)_2Te_3$ (VBST) device, the polarity of SOT switching is modulated by the orientation of the in-plane assisting magnetic field when current pulses are injected along the +x direction.[95] The charge-spin conversion efficiency of all-vdW Sn-doped $Bi_{1.1}Sb_{0.9}Te_2S_1$ (Sn-BSTS)/FGaT heterostructure reaches 1.65 nm^{-1} at room temperature (Fig. 2(f)), far exceeding that of Pt-based counterparts.[96] Nevertheless, field-free SOT switching remains unachievable.

Table 1 summarizes magnetization switching performance of diverse SOT devices under in-plane magnetic fields. It highlights core parameters including switching current density, SOT efficiency and required in-plane magnetic field. None of the listed structure can realize field-free SOT magnetization switching. These structures include magnetron-sputtered thin-film heterostructures (Pt/Py,[18] Pt/Co/AlO_x,[19] Ta/CoFeB/MgO,[17, 97] $PtTe_2$/Au/CoTb[98]), HM/vdW-FM heterostructures (Pt/FGeT,[85, 86] Pt/FGaT[93, 99]), and TI/FM devices.[30, 32, 81, 82, 84, 94-96, 100, 101] One critical bottleneck for the majority of SOT devices is the necessity of an in-plane auxiliary magnetic field (weak or strong) for triggering magnetization switching. For this reason, future research aims to generate OOP torque intrinsically via material design, enabling field-free SOT magnetization switching.

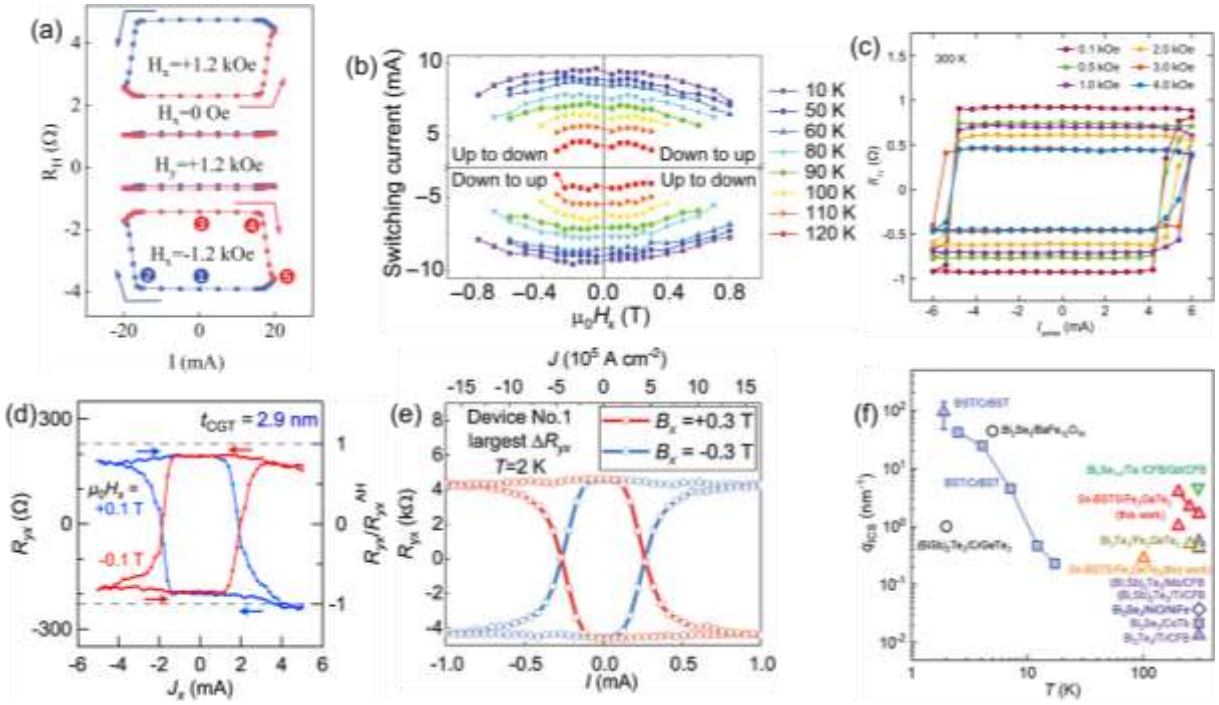


Fig. 2. Current-induced magnetization switching and charge-to-spin conversion in magnetic heterostructures. (a) Hall resistance versus pulsed current for $L1_0$-FePt Hall bars, acquired under field-free and in-plane assisting fields of ±1.2 kOe (along the x-axis) and +1.2 kOe (along the y-axis). Bidirectional deterministic SOT switching is can only be realized with an external in-plane magnetic field. Reprinted with permission from Ref. [89]. Copyright 2020 Wiley-VCH GmbH. (b) SOT switching phase diagram of FGT/Pt bilayers, mapping critical switching current against in-plane magnetic field from 10 to 120 K. The critical current decreases monotonically with rising temperature. A 1 mA drive current corresponds to a current density of 1.85×10^{10} A/m^2 in the Pt layer. Reprinted with permission from Ref. [86] under the terms of the CC-BY 4.0 license. (c) Tuning of current-induced anomalous Hall resistance hysteresis by in-plane magnetic field magnitude in FGaT/Pt devices at 300 K. Both switching threshold and Hall signal amplitude evolve systematically over 0.1-4.0 kOe, verifying field-tunable room-temperature SOT switching. Reprinted with permission from Ref.[93] under the terms of the CC-BY 4.0 license. (d) Current-driven magnetization switching in a 2.9 nm CGT/6 nm BST vdW heterostructure at 2 K, probed via Hall resistance under in-plane magnetic field $\mu_0 H_x = \pm 0.1$ T. The right axis gives the normalized switching ratio R_{yx}/R_{yx}^{AH}, where the dashed horizontal line marks full magnetization reversal. Reprinted with permission from Ref. [94] under the terms of the CC-BY 4.0 license. (e) Hall resistance R_{xy} post each write pulse plotted against pulse amplitude and current density, measured at 2 K with an in-plane assisting field $B_x = \pm 0.3$ T in VBST device. Reprinted with permission from Ref. [95]. Copyright 2024 Wiley-VCH GmbH. (f) Temperature evolution of charge-to-spin conversion efficiency q_{ICS} in BST-family TI devices. Results from second-harmonic (high/low field), hysteresis shift, current-induced switching, and spin-torque ferromagnetic resonance (ST-FMR) methods collectively reveal temperature-dependent spin transport governed by TSS. Reprinted with permission from Ref. [96] under the terms of the CC-BY 4.0 license.

Table 1. Comparison of magnetization switching conditions of SOT devices under in-plane magnetic field[a]

SOT heterojunction	Methods	Thickness (nm)		J_c (A/cm^2)	SOT Ratio (%)	ξ	H_x (Oe)	T (K)	I (mA)	Ref.
		FM layer	SOC layer							
Pt/Co/AlO_x	MS	Co (6)	Pt (20)	N/A	N/A	N/A	100	300	N/A	[19]
Ta/CoFeB/MgO	MS	CoFeB (0.8)	Ta (2)	6.55×10^6	N/A	-0.26	400	300	0.11	[97]
$Pt_{0.75}Ti_{0.25}/Fe_xTb_{1-x}$	MS	Fe_xTb_{1-x} (8)	$Pt_{0.75}Ti_{0.25}$ (5.6)	2.2×10^6	N/A	0.38 ± 0.02 (x=1)	N/A	350	N/A	[102]
$In_{0.3}Ga_{0.7}As/(Ga_{0.94},Mn_{0.06})As$	MBE	$(Ga_{0.94},Mn_{0.06})As$ (15)	$In_{0.3}Ga_{0.7}As$ (500)	4.6×10^4	N/A	N/A	500	N/A	N/A	[103]
$PtTe_2$/Au/CoTb	MS	CoTb (6)	$PtTe_2$ (10)	3.1×10^6	N/A	N/A	2000	N/A	20	[104]
Pt/FGeT	ME/MS	FGeT (87)	Pt (6)	1.85×10^6	N/A	N/A	500	100	1	[86]
Pt/FGeT	ME/MS	FGeT (15-23)	Pt (5)	2.5×10^7	N/A	0.14 ± 0.01	N/A	225	2.4	[85]
BST/CGT	MBE	CGT (12)	BST (6)	N/A	88	1.4	1000	2	2	[94]
Pt/FGaT	ME/MS	FGaT (20)	Pt (6)	1.3×10^7	40	0.22	2000	300	6.3	[99]
Pt/FGaT	ME	FGaT (57.9)	Pt (6)	1.69×10^6	N/A	0.093	100	320	5.4	[93]
FGaT	ME	FGaT (12-28)	N/A	1.7×10^5	95	N/A	80	300	N/A	[105]
Bi_2Se_3/CoTb	MBE/MS	CoTb (4.6)	Bi_2Se_3 (7.4)	1×10^6	N/A	0.16 ± 0.02	800	300	N/A	[82]
Bi_2Se_3/CoFeB	MBE/MS	CoFeB (7)	Bi_2Se_3 (20)	5.7×10^5	N/A	1-1.75	N/A	300	N/A	[100]
Bi_xSe_{1-x}/CoFeB	MBE/MS	CoFeB (5)	Bi_xSe_{1-x} (4, 6, 8, 16, 40)	4.3×10^5	N/A	18.62	80	300	8.5	[84]
$L1_0$ FePt	MS	$L1_0$ FePt	N/A	1×10^7	N/A	N/A	1200	300	0.5	[89]
Bi_2Te_3/MnTe	MBE	MnTe (20)	Bi_2Te_3 (8)	N/A	100	N/A	400	90	N/A	[81]
Bi_2Te_3/FGeT	MBE	FGeT (3)	Bi_2Te_3 (8)	2.2×10^6	N/A	2.69	N/A	300	N/A	[101]
Sn-BSTS/FGaT	VBT/ME	FGaT (11 L)	Sn-BSTS (32)	0.91×10^6	N/A	5.77	1000	300	1.5	[96]
BST/FGeT	MBE/ME	FGeT (2)	BST (10)	1.2×10^6	50	1	2000	100	3.5	[106]
VBST	MBE	VBST	N/A	2.8×10^5	60	N/A	3000	2	N/A	[95]
$Pt/Fe_{0.8}Gd_{0.2}/Ta$	MS	$Fe_{0.8}Gd_{0.2}$ (20-200)	Pt (3)、Ta (3)	$3\text{-}6 \times 10^7$	100	0.38	1000	300	N/A	[107]

[a]Abbreviations: MBE: Molecular Beam Epitaxy. ME: Mechanical Exfoliation. MS: Magnetron Sputtering. EBE: Electron Beam Evaporation. EB: Exchange Bias. IEC: Interlayer Exchange Coupling. VBT: Vertical Bridgman Technique. PLD: Pulsed Laser Deposition. SHH: Second Harmonic Hall.

3. Extrinsic symmetry-breaking field-free SOT switching schemes

To eliminate external magnetic field dependence, early research mainly relies on artificially introducing static structural or magnetic asymmetry to break the switching energy degeneracy, with four representative engineering routes summarized in Fig. 3.

Structural asymmetry is a straightforward way to achieve field-free switching. As shown in Fig. 3(a), Yu et al. introduced a lateral oxidation wedge in Ta/CoFeB/TaOx devices. This breaks the in-plane mirror symmetry and generates an OOP effective field, allowing SOT switching without an external field.[29] Vertical composition gradients within the magnetic layer itself can also break symmetry. In fig. 3(b), Zheng et al. engineered a CoTb film with a gradient-driven Dzyaloshinskii-Moriya interaction (DMI), which dynamically breaks the symmetry during switching, thus eliminating the need for an external field.[32] Similarly, in Pt/FGaT heterostructure, Yun et al. designed an asymmetric device where Pt covers only one edge of the FGaT flake (Fig. (c)).[40] This geometry produces OOP spin currents, also enabling field-free SOT switching. Yet precise multi-layer co-sputtering adds fabrication complexity, and the gradient strength restricts switching efficiency.

Intrinsic properties of vdW magnets have been exploited to simplify device design. For example, in Fig. 3(d), Oh et al. used an IrMn/CoFeB/MgO stack, where the antiferromagnetic (AFM) IrMn layer not only provides SOT but also supplies an exchange bias field. This bias breaks the symmetry, so no external field is needed.[33] A similar concept is demonstrated by Fukami et al. using PtMn/[Co/Ni] multilayers (Fig. 3(e)), where the exchange bias from the device enables field-free SOT switching.[34] In CrSBr/FGeT heterostructure (Fig. (f)), the in-plane exchange bias from the AFM/FM tilts the magnetization of FGeT.[35] Exchange bias from AFM/FM heterostructures offers another effective route. It is worth noting that the exchange bias field from AFM layers such as IrMn, PtMn, and CrSBr are typically oriented in-plane, while this in-plane field can still assist perpendicular SOT switching through a tilting mechanism. Specifically, the in-plane exchange bias field competes with the OOP magnetic anisotropy of the ferromagnetic layer, tilting the magnetization from the perpendicular direction and generating a finite in-plane component. This tilted magnetic configuration breaks

the mirror symmetry of the system and provides the necessary OOP torque component for deterministic SOT switching, effectively replacing the function of an external in-plane magnetic field. Similarly, compared with FGeT, Fe_5GeTe_2 has a canted magnetic anisotropy due to the disorder of Fe lattice (Fig. 3(g)).[36] This provides the necessary symmetry breaking intrinsically, so no auxiliary field or complex geometry is required. Furthermore, in vdW magnet $(Co_{0.5}Fe_{0.5})_{5-x}GeTe_2$ material, Co doping introduces coexisting FM and AFM orders (Fig. 3(h)).[37] This coexistence gives rise to intrinsic exchange bias and canted magnetization, allowing highly efficient field-free SOT switching. In $(Co_{0.15}Fe_{0.85})_5GeTe_2$/Pt heterostructures (Fig. 3(i)), the interface between $(Co_{0.15}Fe_{0.85})_5GeTe_2$ and Pt modifies the magnetic anisotropy and enhances the DMI, which introduces magnetization canting away from the in-plane easy axis.[38] This interface-induced canted magnetization provides the necessary symmetry breaking for field-free SOT switching.

To quantitatively compare the comprehensive performance of extrinsic symmetry-breaking strategies for field-free SOT switching. We summarize the key device indicators in Table 2, including critical switching current, SOT efficiency, operating temperature and specific strategies. Wedge-induced structural asymmetry enables the utilization of mature conventional materials and fabrication methods, but it is limited by unsatisfactory scalability and the necessity of high-precision thickness control. Composition gradients can realize wafer-scale uniformity and flexible performance tunability, whereas their fabrication relies on complex multi-source co-sputtering techniques and precise composition regulation. The exchange bias effect of AFM/FM heterostructures possesses a simple working mechanism and excellent compatibility with mainstream thin-film deposition processes, yet it is restricted by poor thermal stability and precise manipulation of AFM layer properties. The strategy based on canted magnetic anisotropy can realize the simplest device configuration without additional functional layers, nevertheless it is highly dependent on specific materials inherent properties, resulting in limited universality and tunability in practical applications. In summary, these diverse strategies—using structural asymmetry, composition gradients, exchange bias and canted magnetization—all effectively remove the need for an external magnetic field in SOT switching. Nevertheless, these strategies possess inherent drawbacks. More importantly, all the

above strategies depend on post-fabrication artificial modification rather than intrinsic crystal symmetry of spin-source materials. They will degrade switching speed, thermal stability or process compatibility.[35, 36, 40-42, 108, 109] Therefore, we urgently need intrinsically low-symmetry vdW spin-sources to achieve native OOP spin polarization without artificial engineering.

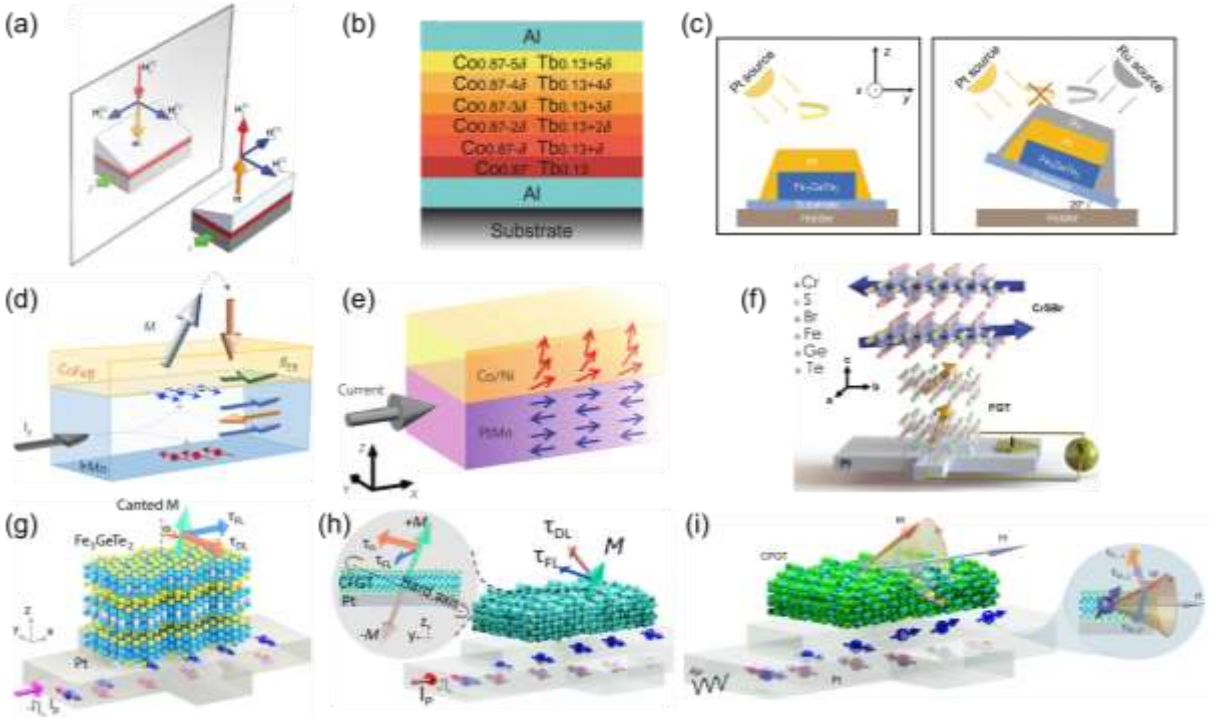


Fig. 3. Structural designs and underlying mechanisms of SOT magnetic heterostructures. (a) OOP effective (H_Z^{FL}) and its mirror image ($H_Z^{FL'}$) generated by lateral asymmetric structure. Unconventional torque caused by transverse symmetry breaking, thus realizing field-free SOT magnetization reversal. Reprinted with permission from Ref. [29]. Copyright 2014 Springer Nature. (b) Layer architecture of composition-graded CoTb films. Continuously graded Co and Tb concentrations (parameterized by δ) along the growth direction are engineered to introduce intrinsic symmetry breaking for field-free SOT operation. Reprinted with permission from Ref. [32] under the terms of the CC-BY 4.0 license. (c) Deposition geometries for symmetric (left) and asymmetric (right) Pt/FGaT devices. The asymmetric structure is fabricated via oblique-angle sputtering of Pt with a Ru capping layer, introducing structural asymmetry. Reprinted with permission from Ref. [40] under the terms of the CC-BY 4.0 license. (d) Schematics of an IrMn/CoFeB bilayer device. The exchange-bias field originating from the AFM/FM interface provides a built-in symmetry-breaking field for deterministic SOT switching. Reprinted with permission from Ref. [33]. Copyright 2016 Springer Nature. (e) PtMn/Co/Ni AFM/FM heterostructure with PMA. Interfacial exchange coupling tilts the Co/Ni magnetic moments near the AFM boundary, establishing an in-plane effective field without an external magnetic field. Reprinted with permission from Ref. [34]. Copyright 2016 Springer Nature. (f) vdW FGT/CrSBr heterostructure dry-transferred onto a Pt Hall-bar for SOT switching measurements. Reprinted with permission from Ref. [35]. Copyright 2024 Wiley-VCH GmbH. (g) Pt/Fe_5GeTe_2 vdW device for current-

driven magnetization switching. Pulsed current (I_P) flows through Pt to generate spin currents via the SHE, exerting both damping-like (τ_{DL}) and field-like (τ_{FL}) torques on the vdW ferromagnet Fe_5GeTe_2. Reprinted with permission from Ref. [36]. Copyright 2025 American Chemical Society. (h) Pt/$(Co_{0.5}Fe_{0.5})_{5-x}GeTe_2$ vdW heterostructure configured for pulsed-current SOT characterization. The inset illustrates the field-free switching mechanism: canted magnetic moments break rotational symmetry, enabling deterministic magnetization reversal without an in-plane auxiliary magnetic field. Reprinted with permission from Ref. [37]. Copyright 2025 Wiley-VCH GmbH. (i) Pt/$(Co_{0.15}Fe_{0.85})_5GeTe_2$ heterostructure under radio-frequency excitation, where SOTs and an external in-plane magnetic field drive coherent magnetization oscillation. The inset depicts multidirectional spin currents arising from both conventional and unconventional SOT contributions at the low-symmetry vdW interface. Reprinted with permission from Ref. [38]. Copyright 2026 American Chemical Society.

Table 2. Parameter comparison of field-free SOT switching realized by different extrinsic symmetry-breaking strategies[a]

SOT heterojunction	Methods	Thickness (nm)		J_c (A/cm^2)	SOT Ratio (%)	ξ	T (K)	I (mA)	∠I and a-axis	strategies	P (W/m^3)	σ ($\hbar$/2e) (Ω·m)$^{-1}$	Ref.
		FM layer	SOC layer										
Ta/CoFeB/TaO_x	MS	CoFeB (1)	Ta (5)	N/A	N/A	N/A	300	N/A	N/A	Wedge (TaOx)	N/A	N/A	[29]
Ta/CoFeB/MgO/TaO_x	MS	CoFeB (wedge)	Ta (5)	2.5 ×10^6	N/A	N/A	300	N/A	N/A	Wedge (CoFeB)	N/A	3	[31]
Pt/FGaT	ME/MS	FGaT (15)	Pt (7)	4.8 ×10^6	45	N/A	300	N/A	N/A	Wedge (Pt)	N/A	N/A	[40]
Ta/MgO/CoFeB	MS	CoFeB (1)	Ta (5)	2.3 ×10^7	N/A	N/A	300	3	N/A	Wedge (MgO)	N/A	N/A	[30]
CoTb	MS	CoTb (6)	N/A	9 ×10^6	N/A	0.061 ± 0.006	300	N/A	N/A	Composition gradient	N/A	N/A	[32]
Pt/Fe: MoS_2	LPCVD /MBE	Pt (8)	Fe: MoS_2 (0.8)	7 ×10^4	N/A	N/A	380	N/A	N/A	Strain induction	7.5 ×10^{12}	N/A	[110]
$LaAlO_3$/$GaRuO_3$	PLD	Py (6)	$GaRuO_3$ (10)	6.3 ×10^6	N/A	0.0086	300	9	0°	Strain induction	N/A	2.59 ×10^2	[111]
Ta/Pt/PtMn/$[Co/Ni]_2$/Co /MgO/Ta	MS	[Co (0.3)/Ni (0.6)]$_2$/Co (0.3)	PtMn (2-8.5)	2.4 ×10^5	N/A	N/A	300	1	N/A	EB	N/A	N/A	[34]
Ta/IrMn/CoFeB/MgO	MS	IrMn (9)/CoFeB (1)	Ta (5)	N/A	N/A	N/A	300	N/A	N/A	EB	N/A	N/A	[33]
Pt/FGeT/CrSBr	ME/MS	FGeT (9)/CrSBr (30)	Pt (10)	N/A	N/A	N/A	30	N/A	N/A	EB	N/A	N/A	[35]
Ta/Pt/CoFe/Ru/CoFe/IrMn/Pt	MS	CoFe (0.8); CoFe (1.5)	Pt (5)	1.5 ×10^6	N/A	0.112	300	2	N/A	IEC	N/A	N/A	[43]
MgO/CoFeB/Ta/CoFeB /MgO	MS	CoFeB (1); CoFeB (1.4)	Ta (1.3)	N/A	100	N/A	300	N/A	N/A	IEC	N/A	N/A	[112]
CoFeB(NiFe)/Ti/CoFeB /MgO	MS	Top-CoFeB (1); bottom-CoFeB (4)	N/A	N/A	N/A	0.014 ± 0.001	300	N/A	N/A	trilayer nonlocal SOT	N/A	N/A	[39]

CoFeB/Ti/CoFeB	MS	Top-CoFeB (1); bottom-CoFeB (4)	N/A	1.2×10^7	90	N/A	300	N/A	N/A	trilayer nonlocal SOT	N/A	N/A	[42]
$L1_2$-Mn_3Ir/(Py/CoFeB)	MS	Py (6)/CoFeB (0.95)	$L1_2$-Mn_3Ir (8)	6.93×10^6	100	0.0214	300	0.77	45°	Tilting magnetic moment	N/A	1.43×10^4	[41]
Bi_2Te_3/Fe_4GeTe_2	MBE/BE	Fe_4GeTe_2 (4)	Bi_2Te_3 (12)	1.55×10^6	16.8	0.8	300	15	N/A	Tilting magnetic moment	N/A	N/A	[79]
Pt/Fe_5GeTe_2	ME/MS	Fe_5GeTe_2 (N/A)	Pt (10)	1.9×10^7	N/A	0.12	300	10	N/A	Tilting magnetic moment	10^{16}	3×10^5	[36]
Pt/$(Co_{0.5}Fe_{0.5})_{5-x}GeTe_2$	ME/EBE	$(Co_{0.5}Fe_{0.5})_{5-x}GeTe_2$ (30)	Pt (10)	8×10^6	N/A	N/A	300	N/A	N/A	Tilting magnetic moment	10^{15}	3×10^5	[37]
Pt/$(Co_{0.15}Fe_{0.85})_5GeTe_2$	ME/EBE	$(Co_{0.15}Fe_{0.85})_5GeTe_2$ (15)	Pt (10)	N/A	N/A	0.010 ± 0.001	300	1.78	N/A	Tilting magnetic moment	N/A	1.6×10^6	[38]

4. Intrinsic OOP spin polarization from low-symmetry vdW spin-sources

Extrinsic symmetry-breaking strategies inevitably introduce extra fabrication complexity and performance tradeoffs. Another powerful approach to achieve field-free switching is to use spin-source materials with low crystal symmetry. By contrast, low-symmetry vdW crystals such as WTe_2, $TaIrTe_4$ and $NbIrTe_4$ can intrinsically generate OOP spin polarization along specific crystal axis, yielding unconventional damping-like torque (τ_{OP}^{AD}) to realize fully field-free deterministic perpendicular magnetization switching without structural modification or external bias.

Owing to its unique ($Pmn2_1$) crystal structure, WTe_2 serves as the most representative material in this category: it retains mirror symmetry along the *bc* plane while breaking mirror symmetry on the ac plane. This anisotropic symmetry constraint creates axis-dependent spin transport behavior (Fig. 4(a)). As shown in Fig. 4(b), when current flows along the low-symmetry *a*-axis of WTe_2, the anomalous Hall effect (AHE) loop shifts clearly with current polarity, indicating a strong OOP damping-like torque. In contrast, when current flows along the high-symmetry *b*-axis (Fig. 4(c)), no loop shift is observed. This symmetry-dependent behavior directly confirms the presence of *z*-spins along the *a*-axis.[55] Using this effect, deterministic field-free switching of the perpendicular vdW magnet FGeT is achieved at low temperatures. Building on this concept, researchers have pushed the operating temperature higher. In Figs. 4d and 4e, the WTe_2/FGaT heterostructure shows clear field-free switching loops at room temperature and even up to 325 K with current applied along the *a*-axis.[48]

Single-layer WTe_2 suffers from limited spin Hall conductivity (SHC), which raises critical switching current and power consumption. To resolve this bottleneck, composite vdW spin-source heterostructures such as $PtTe_2$/WTe_2 have been developed. Centrosymmetric $PtTe_2$ possesses three-fold in-plane rotational symmetry and cannot generate OOP SHC, yet it delivers ultrahigh in-plane SHC ($\sigma_{s,\,y}$). Stacking $PtTe_2$ with low-symmetry WTe_2 enables interlayer spin-to-spin conversion (Fig. 4(f) inset): high-yield in-plane spins generated in $PtTe_2$ are injected into WTe_2, where broken crystal symmetry converts a portion of in-plane spins into OOP spin polarization. This synergistic effect boosts both in-plane SHC ($\sigma_{s,\,y}$) and OOP

SHC ($\sigma_{s,z}$) simultaneously. Compared with pure WTe_2, $PtTe_2/WTe_2$ bilayers (Fig. 4(f)) achieve ~17 times higher in-plane SHC and ~8 times higher OOP SHC, cutting switching power by up to 67 times in Pt-based devices. Micromagnetic simulations further verify that larger spin canting angles enhance the magnitude of τ_{OP}^{AD}, drastically lowering the threshold current density for field-free reversal.[113] Moreover, this bilayer structure supports ultrafast operation (Figs. 4(g) and 4(h)): sub-nanosecond field-free switching is demonstrated with a writing energy of only 0.11 mJ/cm^2, which is 13 times lower than previous reports. The z-spin concept has also been extended to magnon-based systems.[78] Additional, in $PtTe_2/WTe_2$/NiO/CoFeB heterostructures, magnon currents carry both in-plane and OOP spin polarizations through the insulating AFM NiO layer. When current flows along the *a*-axis of WTe_2, the OOP magnon torque enables field-free switching of perpendicular CoFeB with a critical current density of only 4×10^6 A/cm^2. By adding a $PtTe_2$ layer, the power consumption is reduced by 190 times compared to TI-based systems.[114]

Low-symmetry materials like WTe_2 provide a clean and effective route to generate OOP spins for field-free SOT switching. When combined with high-conductivity layers such as $PtTe_2$, these systems achieve both low power and high speed, making them promising for future memory technologies.

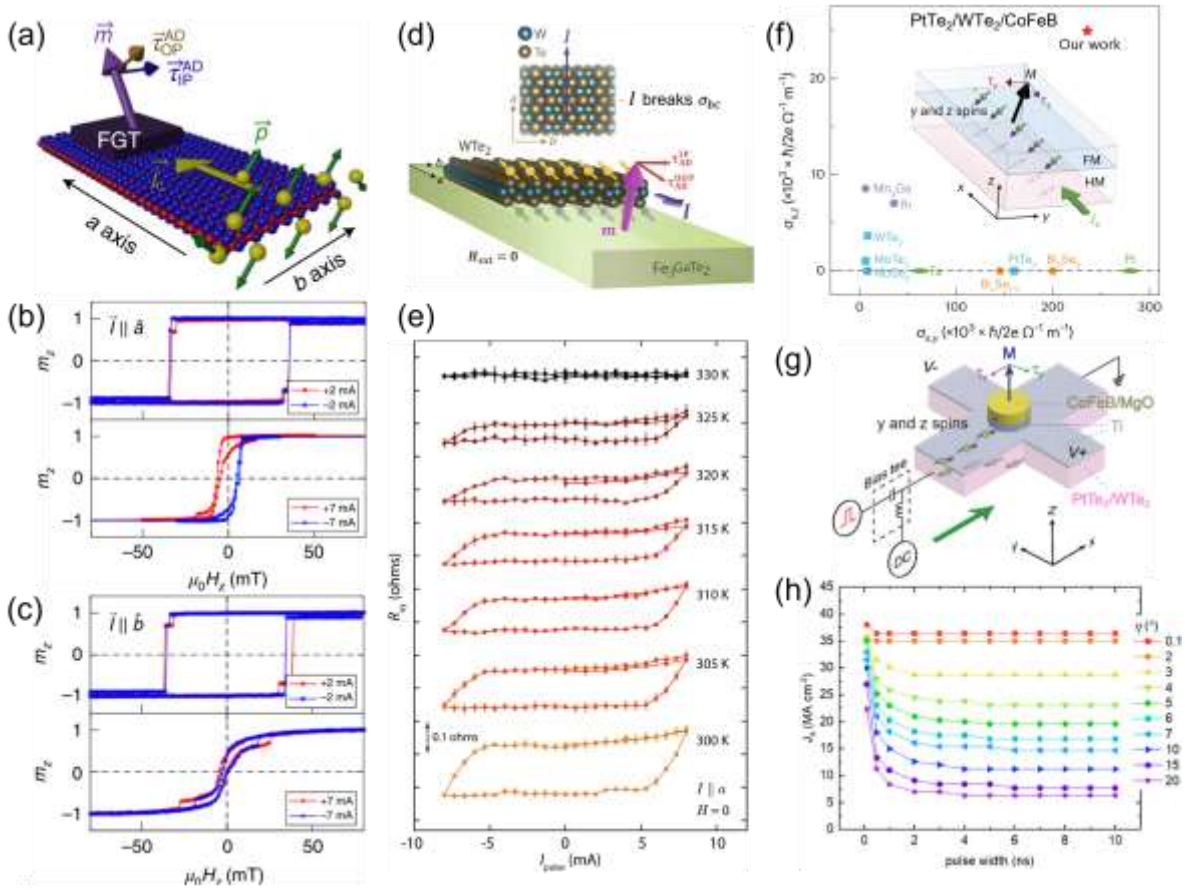


Fig. 4. Field-free SOT switching of WTe_2 in low-symmetry vdW spin-source materials systems. (a) Spin polarization distribution in WTe_2 under current flowing along the *a*-axis. Reduced crystal symmetry breaks the conventional in-plane spin polarization constraint, giving rise to a finite OOP spin component (green arrows) and the associated OOP damping-like SOT. Reprinted with permission from Ref. [55]. Copyright 2022 Springer Nature. (b, c) AHE hysteresis loops measured under OOP magnetic fields with current applied along the *a*-axis and *b*-axis, respectively. The loops shift oppositely for positive and negative current biases, directly evidencing a current-induced OOP effective field. Reprinted with permission from Ref. [55]. Copyright 2022 Springer Nature. (d) Operating principle of field-free deterministic switching in a WTe_2/FGaT heterostructure. Current injection along the low-symmetry *a*-axis breaks mirror symmetry, generating a directionally asymmetric OOP damping-like torque that eliminates the need for in-plane assist field. Reprinted with permission from Ref. [48] under the terms of the CC-BY 4.0 license. (e) Field-free SOT switching of a WTe_2/FGaT device, characterized at temperatures from 300 to 330 K. Traces are vertically offset for clarity. Reprinted with permission from Ref. [48] under the terms of the CC-BY 4.0 license. (f) Benchmark of in-plane ($\sigma_{s,\,y}$) and OOP ($\sigma_{s,\,z}$) SHC for $PtTe_2/WTe_2$ heterostructure relative to established spin-source materials. Inset: device schematic showing how *z*-polarized spins exert an OOP damping-like torque to enable field-free SOT switching in HM/FM bilayer. Reprinted with permission from Ref. [113]. Copyright 2024 Springer Nature. (g) Schematic of the electrical measurement architecture for a $PtTe_2/WTe_2$/Ti/CoFeB/MgO nanopillar device, illustrating the decomposition of applied SOT into in-plane (τ_y) and OOP (τ_z) components. Reprinted with permission from Ref. [78]. Copyright 2025 Wiley-VCH GmbH.

(h) Simulated switching current density J_s as a function of pulse width τ_p across spin polarization canting angles η from 0.1° to 20°, demonstrating that tilted spin polarization substantially reduces switching current density at short pulse durations. Reprinted with permission from Ref. [78]. Copyright 2025 Wiley-VCH GmbH.

Compared with binary low-symmetry vdW materials such as WTe_2, ternary type-II Weyl semimetals $TaIrTe_4$ and $NbIrTe_4$ possess enhanced intrinsic Berry curvature dipole and large OOP SHC. Benefiting from the robust unconventional SOT, room-temperature deterministic field-free magnetization switching has been experimentally demonstrated in their heterostructures.[44-46, 59-62]

Figs. 5(a) and 5(b) show that $TaIrTe_4$/CoFeB device exhibit a large OOP SOT efficiency ($\xi_{SOT}^{a\text{-axis}} \approx 0.05$) and field-free switching with a critical current density of 2.35×10^6 A/cm^2 at room temperature.[60] Figs. 5(c) and 5(d) display angle-resolved ST-FMR signals of $TaIrTe_4$/NiFe devices. For *a*-axis oriented devices, the symmetric and antisymmetric resonance curves deviate from the standard $\sin2\Phi\cos\Phi$ fitting function of HM systems, with nonzero coefficients directly proving the existence of unconventional SOT-induced OOP Field-like and damping-like.[61] Loop shift anomalous Hall measurements directly visualize the effective magnetic field induced by unconventional SOT (Figs. 5(e) and 5(f)). Under large dc current along the *a*-axis, the hysteresis loop produces an obvious horizontal offset, corresponding to an OOP effective field of 2.2 mT/(1×10^6 A/cm^2) and SOT efficiency of 0.37; no measurable loop shift appears for *b*-axis currents.[46] Room-temperature field-free deterministic switching characteristics of $TaIrTe_4$/FGaT all-vdW heterostructure are shown in Figs. 5(g-i). Combining second-harmonic Hall spectroscopy and current-driven switching characterization, we quantify the room-temperature performance of $TaIrTe_4$/FGaT all-vdW heterostructure, achieving a low critical switching current density of 1.81×10^6 A/cm^2 and low power density of 0.348×10^{15} W/m^3, whose SHC and power consumption are benchmarked against prevailing SOT systems in Fig. 5(h). The OOP damping-like effective field H_{DL}^{Z} exhibits prominent temperature tunability (Fig. 5(i)), falling from 2 K to a valley at 100-200 K before rising again up to 325 K; this trend originates from temperature-modulated Fermi level (E_F) shifts that regulate the magnitude of OOP spin accumulation in $TaIrTe_4$, verifying the chemical potential as an intrinsic

knob to tailor unconventional SOT strength.[45]

More recently, $NbIrTe_4$ has emerged as another candidate. As shown in Figs. 5(j) and 5(k), $NbIrTe_4$ enhances the OOP SHC ($\sigma_{s,z}$) by over fourfold, reaching 1.2×10^5 $(\hbar/2e)(\Omega\cdot m)^{-1}$, which exceeds the in-plane component. The spin tilt angle increases from 11° to 77°, marking a transition to OOP dominant spin transport. This large $\sigma_{s,z}$ enables field-free switching with an low current density of 1.4×10^6 A/cm^2 and a power consumption of only 0.29 mW/μm^3, which is 200 times lower than Pt-based systems.[62] Among three CoFeB-based devices with the same ferromagnetic-layer thickness, the $NbIrTe_4$ (24 nm)/CoFeB device achieves a switching power consumption of 7.077 mW. Under identical device architectures and measurement conditions, this value is 16 times lower than that of WTe_2 (25 nm)/CoFeB (115.439 mW) and 4 times lower than that of $TaIrTe_4$ (22 nm)/CoFeB (26.263 mW). Figure 5(l) further supports this result, which shows a higher switching efficiency and a larger critical field for the $NbIrTe_4$ device compared with the WTe_2 and $TaIrTe_4$ devices.

The switching speed and power consumption of field-free SOT devices are dependent on the orientation and magnitude of spin polarization. From the perspective of spin orientation, conventional heavy metals only generate in-plane spin polarization ($\sigma_{s,xy}$), for which damping-like torque lies in the film plane and cannot lift the energy degeneracy of perpendicular magnetization states. Deterministic switching in such systems relies on external in-plane magnetic fields or artificial symmetry-breaking structures, which introduce extra energy dissipation and prolong switching dynamics through magnetization precession. In contrast, the OOP spin polarization ($\sigma_{s,z}$) intrinsically generated by low-symmetry vdW crystals exerts a perpendicular damping-like torque directly on the perpendicular magnetic moment. The magnitude of this OOP effective field follows the general scaling relation $H_{DL}^{Z} = \frac{\hbar}{2e}\cdot\frac{\sigma_{s,z}\cdot J_c}{M_s t_{FM}}$,[38, 45, 46, 58, 93] which has been experimentally verified in WTe_2-based heterostructures.[54, 55] This intrinsic symmetry-breaking mechanism eliminates the energy loss and switching delay caused by auxiliary magnetic fields, enabling more efficient and faster magnetization reversal.

From the perspective of magnitude, the critical switching current density (J_c) scales inversely

with $\sigma_{s,z}$, following the relation $J_c \propto \frac{M_s t_{FM} H_k}{\sigma_{s,z}}$.[38, 45, 46, 58, 93] A large OOP spin Hall conductivity delivers a higher OOP spin current density under the same charge current, thus reducing the threshold current for switching. As summarized in Table 3, as $\sigma_{s,z}$ increases from 1.47×10^4 $\hbar/2e\cdot(\Omega\cdot m)^{-1}$[60] to 1.65×10^6 $\hbar/2e\cdot(\Omega\cdot m)^{-1}$[45], J_c decreases from ~2.35×10^6 A/cm^2 to 1.8×10^6 A/cm^2, consistent with the inverse scaling law. For switching speed, the characteristic switching time follows the relation $\tau_s \propto \frac{1}{\sigma_{s,z} \cdot J_c}$.[10, 113] The $PtTe_2/WTe_2$ heterostructure with enhanced $\sigma_{s,z}$ (0.25×10^5 $\hbar/2e\cdot(\Omega\cdot m)^{-1}$) achieves sub-nanosecond field-free switching with an ultra-low writing energy of 0.11 mJ/cm^2, which is 13 times lower than single-layer WTe_2-based devices.[113]

Notably, the energy consumed per magnetization switching event scales approximately as $E_{switch} \propto \frac{1}{\sigma_{s,z}^2}$, meaning that increasing OOP spin Hall conductivity reduces power consumption in a nonlinear manner.[10, 12] For materials systems, a general trade-off exists between switching speed and power consumption. $NbIrTe_4$ possessing a record-high $\sigma_{s,z}$ is highly suitable for ultra-low-power memory applications, while $PtTe_2/WTe_2$ hybrid structures combine high in-plane and OOP SHC to realize ultrafast switching at moderate power. Optimizing both the orientation purity and magnitude of OOP spin polarization via crystal symmetry engineering and interface design will be the core direction for developing next-generation high-speed, low-power field-free SOT devices.

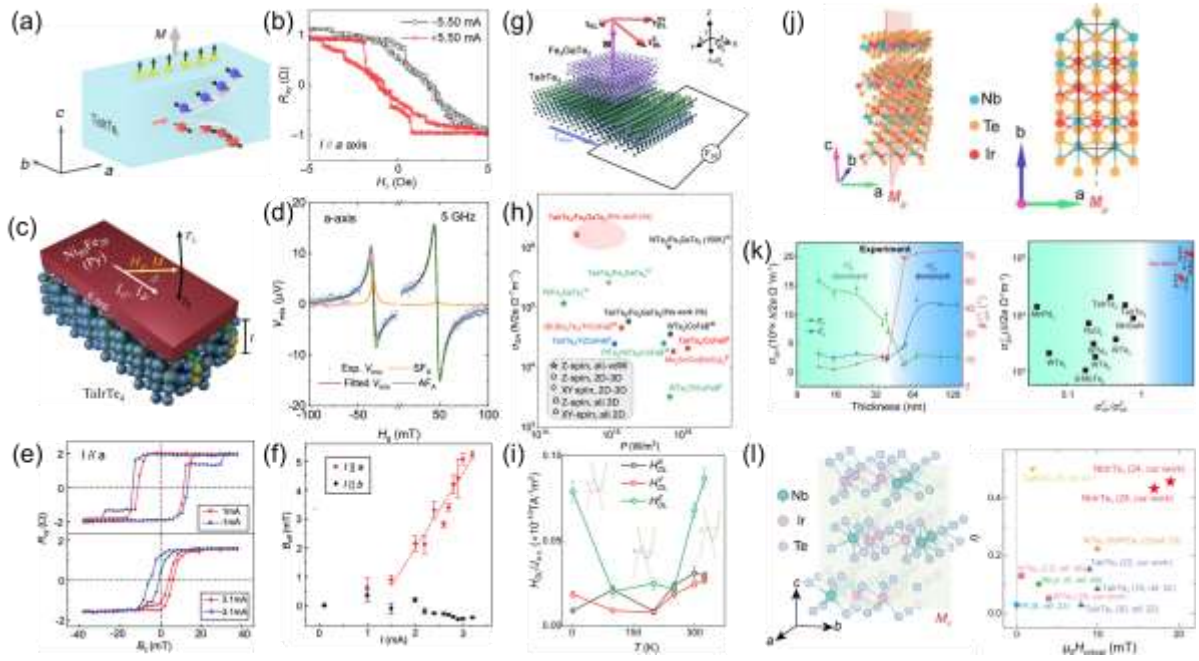


Fig. 5. Unconventional OOP SOT of $TaIrTe_4$ and $NbIrTe_4$ in low-symmetry transition-metal telluride heterostructures. (a) Spin accumulation at the $TaIrTe_4$ surface under current along the crystalline *a*-axis. Broken mirror symmetry along the *a*-axis generates unconventional OOP spin polarization σ_z alongside the conventional in-plane σ_y component. Reprinted with permission from Ref. [60] under the terms of the CC-BY 4.0 license. (b) AHE hysteresis loops of a $TaIrTe_4$/Ti/CoFeB device, recorded at ±5.50 mA bias with current aligned along the *a*-axis. Reprinted with permission from Ref. [60] under the terms of the CC-BY 4.0 license. (c) Schematic of the $TaIrTe_4$/permalloy (Py) heterostructure for ST-FMR characterization, defining the in-plane and OOP damping-like torque components and the azimuthal angle Φ between current and applied magnetic field. Reprinted with permission from Ref. [61] under the terms of the CC-BY 4.0 license. (d) ST-FMR mixing voltage spectra of the *a*-axis $TaIrTe_4$/Py device measured at 5 GHz, with fitted curves decomposed into symmetric (field-like) and antisymmetric (damping-like) Lorentzian contributions. Reprinted with permission from Ref. [61] under the terms of the CC-BY 4.0 license. (e) AHE hysteresis loops of $TaIrTe_4$/FGaT under ±1 mA and ±3.1 mA bias currents along the *a*-axis. Systematic loop shifts at ±3.1 mA verify the existence of a current-induced OOP effective field from unconventional SOT. Reprinted with permission from Ref. [46]. Copyright 2024 Wiley-VCH GmbH. (f) SOT effective field (B_{eff}) as a function of current amplitude for $TaIrTe_4$/FGaT with current along the *a*- and *b*-axes. Robust B_{eff} appears exclusively for $I//a$, whereas negligible B_{eff} values are observed for $I//b$, confirming the symmetry-governed origin of the unconventional torque. Error bars denote standard deviation from three repeated measurements. Reprinted with permission from Ref. [46]. Copyright 2024 Wiley-VCH GmbH. (g) Device schematic of the all-vdW $TaIrTe_4$/FGaT heterostructure under pulsed current injection. The OOP damping-like torque arising from the low-symmetry spin-source materials supports deterministic field-free SOT switching. Reprinted with permission from Ref. [45] under the terms of the CC-BY 4.0 license. (h) Comparison of SHC and power consumption of representative SOT devices. Shaded ellipses indicate device-to-device variation and parameter uncertainty. Reprinted with permission from Ref. [45] under the terms of the CC-BY 4.0 license.

(i) Normalized damping-like effective field $H_{DL}/J_{a.c.}$ versus temperature measured on $TaIrTe_4$/FGaT heterostructures. Insets display the band dispersion of type-II Weyl semimetals and thermally tunable E_F shift. Reprinted with permission from Ref. [45] under the terms of the CC-BY 4.0 license. (j) Crystal structure of $NbIrTe_4$ with $Pmn2_1$ space-group symmetry, illustrating layered atomic stacking configuration and two distinct mirror symmetry operations (simple mirror and glide mirror planes). Reprinted with permission from Ref. [62]. (k) Thickness-dependent evolution of SHC σ_{sh}^{z}, σ_{sh}^{y} and spin canting angle Φ_{spin} extracted from angle-resolved ST-FMR measurements on $NbIrTe_4$/Ti/CoFeB device (left panel); comparative summary of OOP SHC σ_{sh}^{z} and the σ_z/σ_y ratio versus previously reported values (right panel). Reprinted with permission from Ref. [62]. (l) Left: atomic structure of $NbIrTe_4$; Right: comparison of critical switching current density, switching efficiency, and critical in-plane magnetic ($\mu_0 H$) field for various SOT systems. $NbIrTe_4$/CoFeB exhibits the lowest current density (3.6×10^6 A/cm^2) and the highest $\mu_0 H$ (19 mT), demonstrating superior field-free switching robustness among all reported intrinsic low-symmetry materials. Reprinted with permission from Ref. [44]. Copyright 2026 American Chemical Society. Data for other systems are from Ref. [41, 59, 60, 111, 113, 115].

Table 3 summarizes core device parameters of typical intrinsic low-symmetry vdW spin-source materials, covering binary WTe_2 and ternary type-II Wely semimetals $TaIrTe_4$. All these materials rely on inherent broken crystallographic symmetry to generate OOP spin polarization and enable field-free perpendicular magnetization switching without artificial structural modification. In summary, low-symmetry Wely semimetals provide a powerful platform for generating OOP spin currents. Among them, $NbIrTe_4$ stands out with record-high $\sigma_{s,z}$ and the lowest power consumption, making it a highly promising candidate for energy-efficient, field-free SOT memory technologies.

Table 3. Parameter comparison of field-free SOT switching realized by different intrinsic spin-source materials[a]

SOT heterojunction	Methods	Thickness (nm)		J_c (A/cm^2)	SOT Ratio (%)	ξ_x	ξ_y	ξ_z	T (K)	I (mA)	∠I and a-axis	P (W/m^3)	σ ($\hbar/2e$) (Ω·m)$^{-1}$		Origin	Ref.
		FM layer	SOC layer										$\sigma_{s,xy}$	$\sigma_{s,z}$		
$MoTe_2$/Py	ME/MS	Py (6)	$MoTe_2$ (66.1)	6.71×10^5	N/A	N/A	N/A	0.35	300	N/A	N/A	N/A	N/A	5.0×10^4	MOKE	[116]
CuPt/CoPt	MS	CoPt (4)	CuPt (10)	N/A	N/A	N/A	N/A	0.07	N/A	18	0°/60°/120°/180°	N/A	N/A	N/A	SHH/loop shift	[117]
$MnPd_3$/CoFeB	MS	CoFeB (5)	$MnPd_3$ (4-24)	7.5×10^6	N/A	0.017	0.41	0.011	400	9.5	N/A	N/A	2.8×10^4	1.8×10^4	SHH/ ST-FMR	[118]
WTe_2/$CrTe_2$	MBE	$CrTe_2$ (5)	WTe_2 (6)	1.2×10^6	83	N/A	0.14	-0.028	150	N/A	0°	N/A	N/A	N/A	ST-FMR	[119]
WTe_2/Py	ME/MS	Py (6)	WTe_2 (5.5)	N/A	N/A	N/A	N/A	N/A	300	N/A	0°	N/A	8×10^3	3.6×10^3	ST-FMR	[54]
WTe_2/Py	ME/MS	Py (6)	WTe2 (19.6)	2.96×10^5	N/A	N/A	N/A	0.09-0.51	300	N/A	0°	N/A	N/A	N/A	ST-FMR	[120]
$PtTe_2$/WTe_2/CoFeB	MBE/MS	CoFeB (2.9)	$PtTe_2$ (2)/WTe_2 (6)	2.6×10^6	N/A	N/A	0.15	-0.034	300	N/A	0°	N/A	1.335×10^4	-0.3×10^4	ST-FMR	[113]
$PtTe_2$/WTe_2/Ti/CoFeB	MBE	CoFeB (1)	$PtTe_2$ (2)/WTe_2 (6)	12.3×10^6	90	N/A	N/A	N/A	300	N/A	0°	N/A	N/A	N/A	N/A	[78]
WTe_2/FGeT	ME	FGeT	WTe_2 (12.6)	3.9×10^6	N/A	N/A	N/A	4.6	150	1.5	0°	N/A	N/A	N/A	H_c	[56]

		(7.3)														
$WTe_2/Fe_{2.78}GeTe_2$	ME	$Fe_{2.78}GeTe_2$ (4.1)	WTe_2 (25.8)	9.8×10^6	N/A	N/A	N/A	N/A	150	9	0°	N/A	N/A	N/A	N/A	[55]
WTe_2/FGaT	ME	FGaT (17.9)	WTe_2 (23.8)	2.23×10^6	N/A	N/A	N/A	N/A	325	8	0°	N/A	N/A	N/A	N/A	[48]
$TaIrTe_4$/Py	ME/MS	Py (6)	$TaIrTe_4$ (25)	1.6×10^8	N/A	N/A	0.113	0.043	300	N/A	0°	N/A	5.437×10^4	2.065×10^4	ST-FMR	[59]
$TaIrTe_4$/Ti/CoFeB	ME/MS	CoFeB (1.2)	$TaIrTe_4$ (10)	2.35×10^6	0.03	N/A	N/A	0.03	300	N/A	0°	N/A	N/A	1.47×10^4	loop shift	[60]
$TaIrTe_4$/FGaT	ME	FGaT (4.8)	$TaIrTe_4$ (10.3)	2.56×10^6	N/A	N/A	0.15	0.37	300	3.4	0°	N/A	N/A	N/A	loop shift	[46]
$TaIrTe_4$/FGaT	ME	FGaT (49.3)	$TaIrTe_4$ (78.2)	1.81×10^6	100	N/A	N/A	1.76	300	3.5	0°	3.48×10^{14}	N/A	1.65×10^6	loop shift	[45]
$NbIrTe_4$/Ti/CoFeB	ME/MS	CoFeB (1.3)	$NbIrTe_4$ (14-119.6)	1.4×10^6	N/A	N/A	0.26	0.06	300	N/A	0°	2.9×10^{14}	$0.25\text{-}1.75 \times 10^5$	$0.35\text{-}1.2 \times 10^5$	ST-FMR/ loop shift	[62]
$NbIrTe_4$/Ti/CoFeB	ME/MS	CoFeB (1.3)	$NbIrTe_4$ (24)	3.6×10^6	57	N/A	0.011	0.0586	300	N/A	0°	N/A	N/A	2.61×10^4	ST-FMR/ loop shift	[44]
$Co_{1/3}TaS_2$/FGeT	ME	FGeT (16/20/15)	$Co_{1/3}TaS_2$ (40/30/47)	10^6	N/A	N/A	N/A	N/A	90	9	0°-360°	10^{15}	N/A	N/A	SHH	[121]

5. 2D vdW integrated devices: memory, logic and neuromorphic computing

Integrating SOT with 2D vdW materials provides a novel pathway for developing miniaturized, energy-efficient, and non-volatile memory and logic devices. Unlike conventional HM/FM systems, vdW materials offer atomically sharp interfaces, tunable magnetic anisotropy, and compatibility with wafer-scale growth, making them particularly attractive for SOT-MRAM) and spin logic applications.[15, 71, 72, 75-77, 79, 122-124]

A central focus has been the development of field-free magnetization switching, a critical requirement for practical SOT-MRAM integration. One promising approach utilizes perpendicular-anisotropy spin-orbit (PASO) quantum materials, such as WTe_2/FGeT heterostructures. These systems exploit unconventional charge-to-*z*-spin conversion to enable deterministic switching of perpendicular magnetization without an external field. This mechanism also allows for a symmetric readout via the inverse *z*-spin-to-charge conversion, which is essential for creating cascadable logic-in-memory circuits. As demonstrated, a single PASO device can be configured to perform fundamental Boolean operations (NAND, NOR, NOT), showcasing the potential for non-volatile logic (Fig. 6(a)).[75]

Another significant stride has been the realization of room-temperature field-free switching using novel physical phenomena. The orbit-transfer torque (OTT) effect, demonstrated in WTe_2/FGaT heterostructures, utilizes current-induced orbital polarization to achieve highly energy-efficient switching (Fig. 6(b)).[76] This work has culminated in an all-vdW WTe_2/FGaT/*h*-BN/FGaT OTT-MRAM, which exhibits a TMR ratio of 14% at 300 K and robust field-free writing, marking a crucial step toward practical applications. Further expanding the material system, WTe_2/FGeT/WS_2/Cr_3Te_4 devices combine distinct 2D magnets with a thin WS_2 tunnel barrier (Fig. 6(c)). This architecture achieves a very low resistance-area product of 15.5 kΩ·μm^2 and demonstrates low power switching, highlighting the tunability offered by different 2D vdW materials.[15]

Beyond simple magnetization switching, the functional versatility of SOT devices based on 2D vdW materials is being explored. For instance, the intrinsic coexistence of in-plane and PMA in Bi_2Te_3/Fe_4GeTe_2 heterostructures provides an internal symmetry-breaking field,

enabling polarity-tunable field-free switching (Fig. 6(d)). This capability was directly utilized to implement 16 reconfigurable Boolean logic functions in a single device, demonstrating a path toward highly compact and adaptable spin-logic systems.[79] Similarly, the rich physics of the topological insulator Bi_2Te_3 and ferromagnetic $CrTe_2$ has been harnessed to emulate brain-like functions. Devices based on this system exhibit highly linear, multi-state memory behavior suitable for synapses and an intrinsic sigmoidal switching curve for neuronal activation functions, as shown in Fig. 6(e).[77] This integration of synaptic and neuronal functions within a single material system is a foundation for developing low power, on-chip artificial neural networks.

Collectively, these advancements from 2D vdW heterostructures have not only addressed key challenges such as field-free switching and room-temperature operation but have also unveiled opportunities for advanced computing paradigms like logic-in-memory and neuromorphic computing. The progression from basic switching demonstrations to complex functional devices underscores the potential of this material class to redefine the landscape of next-generation spintronic memory and logic systems.

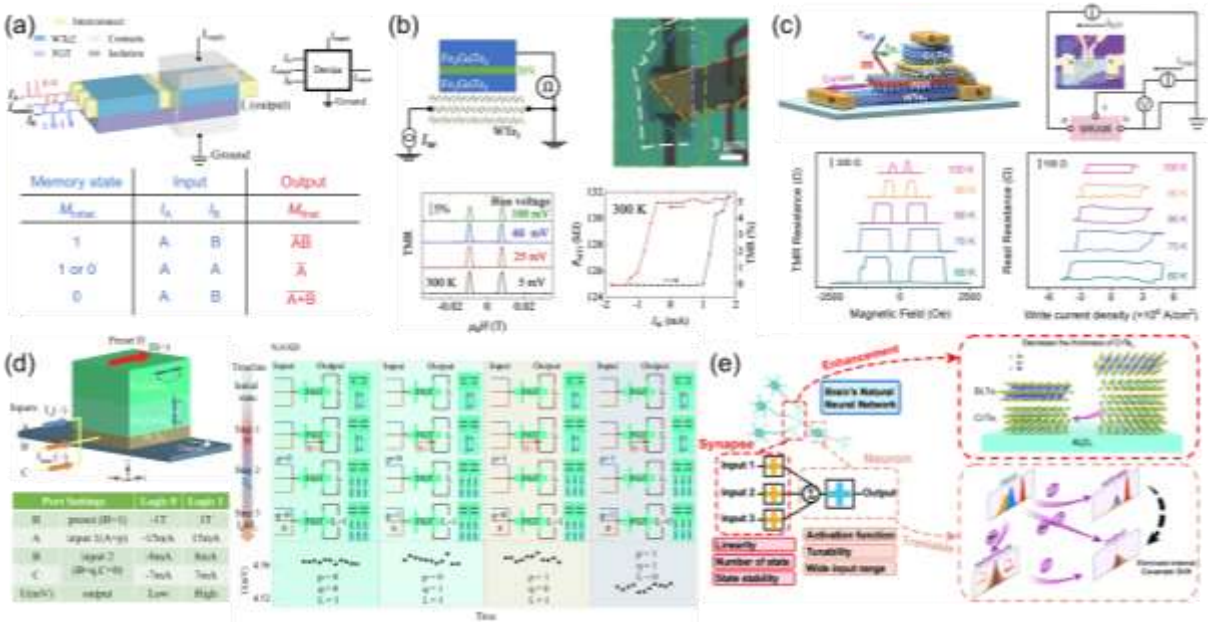


Fig. 6. All-vdW SOT heterostructure devices for in-memory logic, nonvolatile magnetic memory, and neuromorphic computing. (a) PASO logic device built on a WTe_2/FGeT vdW stack. Two input currents I_A and I_B are injected along the transport channel, yielding an output current I_C whose logic state is governed by the initial magnetization of the FGeT ferromagnetic layer. The attached truth table summarizes state-dependent reconfigurable Boolean operations. Reprinted with permission from Ref. [75] under the terms of

the CC-BY 4.0 license. (b) Panels from left to right display: schematic of the WTe_2/FGaT/*h*-BN/FGaT heterostructure, optical micrograph of the patterned device cell, tunneling magnetoresistance curves measured at 300 K, and current-induced SOT switching by pulsed write currents I_W. Reprinted with permission from Ref. [76]. Copyright 2023 Elsevier B.V. (c) All-vdW SOT-MRAM cell constructed upon a WTe_2/FGeT/WS_2/Cr_3Te_4 heterostructure. Top panel: device layout, measurement circuit, and corresponding optical micrograph. Bottom panel: temperature-dependent TMR spectra collected from 60 to 100 K (left) and field-free current-driven magnetization switching characteristics (right). Reprinted with permission from Ref. [15]. Copyright 2025 Wiley-VCH GmbH. (d) Reconfigurable Boolean logic gate based on a Bi_2Te_3/Fe_4GeTe_2 heterostructure. The device uses a preset magnetic field and three independent current inputs to reconfigure the logic function, and this architecture verifies robust NAND logic operation under programmable input configurations. Reprinted with permission from Ref. [79] under the terms of the CC-BY 4.0 license. (e) All-vdW Bi_2Te_3/$CrTe_2$ heterostructures as synaptic building blocks for neuromorphic systems. Left: neural network schematic outlining core requirements for synaptic and neuronal units. Upper right panel: thickness-engineered $CrTe_2$/Bi_2Te_3 stacks designed to deliver tunable synaptic behavior. Lower right panel: the batch normalization algorithm is adopted to suppress internal covariate shift during neural network training. Reprinted with permission from Ref. [77]. Copyright 2024 American Chemical Society.

6. Conclusion and perspectives

SOT has matured over the past several decades from a fundamental spin-transport phenomenon into a versatile platform for non-volatile memory, logic, and neuromorphic computing. This review has traced the evolutionary pathway of SOT-driven perpendicular magnetization switching. It covers the initial reliance on external magnetic fields, the emergence of field-free switching through both extrinsic symmetry breaking and intrinsic material design, and finally to the integration of these capabilities into functional device architectures.

The core limitation of SOT technology lies in the mandatory in-plane magnetic field required for deterministic switching of perpendicular magnetic moments. Multiple complementary strategies have been proposed to address this constraint. Extrinsic approaches, such as lateral structural asymmetry[29-32, 40], exchange bias from AFM/FM[33-35, 43], and tilted magnetic anisotropy[36-38], can effectively eliminate the need for an external magnetic field but often at the cost of architectural complexity and reduced scalability. Moreover, the discovery of intrinsic OOP spin polarization in low-symmetry vdW materials delivers a more physically concise alternative. Representative materials candidates include WTe_2,[47, 48, 50-58] $TaIrTe_4$,[45, 46,

[59-61] and $NbIrTe_4$.[44, 62] Here, the broken mirror symmetry inherent to the crystal structure itself generates *z*-spins when current flows along the low-symmetry axis, enabling field-free switching without any artificial structural modification.

From memory cells to functional circuits. The translation of these materials advances into functional device architectures has proceeded at an equally rapid pace. Three-terminal SOT-MRAM structures offer physically decoupled write and read paths, enhancing endurance and design flexibility.[15] Multifunctional integration within single vdW heterostructure represents another important advance. For example, WTe_2 provides the SOT write mechanism while a FGaT/*h*-BN/FGaT tunnel junction performs signal readout. This stack enables room-temperature all-vdW magnetoresistive memory with TMR ratios exceeding 14%.[76] Beyond conventional memory, the same SOT devices have been reconfigured as synaptic and neuronal units for neuromorphic computing. The demonstration of 16 reconfigurable Boolean logic functions in Bi_2Te_3/Fe_4GeTe_2 devices further illustrates the potential for energy-efficient, compact spin-logic circuits, where field-free switching with polarity control enables complete logic functionality.[79]

Persistent challenges and future directions. Despite these remarkable advances, several challenges remain. First, the scaling of vdW heterostructures to sub-10 nm dimensions and their integration with complementary metal oxide semiconductor (CMOS) circuits is essential for commercial memory and logic applications. This goal calls for mature wafer-scale material growth techniques and reliable large-area transfer methods. Second, despite the power consumption of $NbIrTe_4$-based devices represents a significant milestone, further power reductions will likely require the synergistic combination of intrinsic *z*-spin-sources with high-conductivity materials such as $PtTe_2$ to maximize both the OOP SHC and the charge conductivity simultaneously. Third, the fundamental understanding of spin-to-spin conversion mechanisms at vdW interfaces, particularly the role of orbital moments and the DMI, remains incomplete and warrants systematic experimental and theoretical investigation.

Looking ahead, the convergence of low-symmetry vdW materials, vdW heterostructure engineering, and spintronic device physics points toward an integrated paradigm where SOT not only writes and reads magnetic information but also performs computation directly within

the memory array. Achieving field-free, low-power, and scalable SOT devices based on intrinsic *z*-spin-sources marks a critical step toward this vision. As the material system continues to expand and the understanding of symmetry-controlled spin phenomena deepens, SOT technology is poised to play a central role in the development of energy-efficient, non-volatile computing architectures beyond the von Neumann paradigm.

Acknowledgements

This work is supported by the National Natural Science Foundation of China (U24A6002, 52571263, 52571229, and 12504145), the National Key Research and Development Program of China (2022YFA1204000), the Tianjin Key Research and Development Program (24YFXTHZ00150), and the Natural Science Foundation of Hebei Province (E2026110016 and E2026110036).

Reference

[1] Jiang X, Bao J, Zhang L and Bai L 2022 *Microelectronics J* **121**, 105355
[2] Sousa RC and Prejbeanu IL 2005 *C. R. Physique* **6**, 1013-1021
[3] Ando K, Fujita S, Ito J, Yuasa S, Suzuki Y, Nakatani Y, Miyazaki T and Yoda H 2014 *J. Appl. Phys.* **115**, 172607
[4] Xu Y, Wu B, Wang Z, Wang Y, Zhang Y and Zhao W 2020 *IEEE Trans. Electron Devices* **67**, 1460-1465
[5] Wang Z, Zhao W, Deng E, Klein J-O and Chappert C 2015 *J. Phys. D Appl. Phys.* **48**, 065001
[6] Cui J, Zhang K-X and Park J-G 2024 *Adv. Electron. Mater.* **10**, 2400041
[7] Zhu L, Zhu L, Shi S, Ralph DC and Buhrman RA 2020 *Adv. Electron. Mater.* **6**, 1901131
[8] Lin H, Luo X, Liu L, Wang D, Zhao X, Wang Z, Xue X, Zhang F and Xing G 2022 *Micromachines* **13**, 1-18
[9] Wang M, Cai W, Zhu D, Wang Z, Kan J, Zhao Z, Cao K, Wang Z, Zhang Y, Zhang T, Park C, Wang J-P, Fert A and Zhao W 2018 *Nat. Electron.* **1**, 582-588
[10] Brataas A, Kent AD and Ohno H 2012 *Nat. Mater.* **11**, 372-381
[11] Garello K, Miron IM, Avci CO, Freimuth F, Mokrousov Y, Blügel S, Auffret S, Boulle O, Gaudin G and Gambardella P 2013 *Nat. Nanotechnol.* **8**, 587-593
[12] Sinova J, Valenzuela SO, Wunderlich J, Back CH and Jungwirth T 2015 *Rev. Mod. Phys.* **87**, 1213-1260
[13] Shao Q, Yu G, Lan Y-W, Shi Y, Li M-Y, Zheng C, Zhu X, Li L-J, Amiri PK and Wang KL 2016 *Nano Lett.* **16**, 7514-7520
[14] Qiu X, Shi Z, Fan W, Zhou S and Yang H 2018 *Adv. Mater.* **30**, e1705699

[15] He K, Li B, Nie J, Hou Y, Huan C, Hong M, Du J, Chen Y, Tang J, Yi C, Feng Y, Liu S, Wu S, Liu M, Zhang H, Guo Y, Wu R, Li J, Liu X, Liu Y, Wei Z, Liao L, Li B and Duan X 2025 *Adv. Mater.* **37**, 2419939
[16] Miron IM, Garello K, Gaudin G, Zermatten PJ, Costache MV, Auffret S, Bandiera S, Rodmacq B, Schuhl A and Gambardella P 2011 *Nature* **476**, 189
[17] Liu L, Pai C-F, Li Y, Tseng HW, Ralph DC and Buhrman RA 2012 *Science* **336**, 555-558
[18] Liu L, Moriyama T, Ralph DC and Buhrman RA 2011 *Phys. Rev. Lett.* **106**, 036601
[19] Liu L, Lee OJ, Gudmundsen TJ, Ralph DC and Buhrman RA 2012 *Phys. Rev. Lett.* **109**, 096602
[20] Pai C-F, Liu L, Li Y, Tseng HW, Ralph DC and Buhrman RA 2012 *Appl. Phy. Lett.* **101**, 122404
[21] Emori S, Bauer U, Ahn SM, Martinez E and Beach GSD 2013 *Nat. Mater.* **12**, 611
[22] Haazen PP, Mure E, Franken JH, Lavrijsen R, Swagten HJ and Koopmans B 2013 *Nat. Mater.* **12**, 299
[23] Yun-Chi Zhao GYB-WDS-GWCWYSJ-YZG-HY 2016 *Chin. Phys. B* **25**, 77501-077501
[24] Sha Lu DMAKZWSC and Shiheng L 2024 *Chin. Phys. B* **33**, 107501-107501
[25] You L, Lee O, Bhowmik D, Labanowski D, Hong J, Bokor J and Salahuddin S 2015 *Proc. Natl. Acad. Sci. U. S. A.* **112**, 10310-10315
[26] Manchon A, Železný J, Miron IM, Jungwirth T, Sinova J, Thiaville A, Garello K and Gambardella P 2019 *Rev. Mod. Phys.* **91**, 035004
[27] Kateel V, Krizakova V, Rao S, Cai K, Gupta M, Monteiro MG, Yasin F, Sorée B, De Boeck J, Couet S, Gambardella P, Kar GS and Garello K 2023 *Nano Lett.* **23**, 5482-5489
[28] Shao Q, Li P, Liu L, Yang H, Fukami S, Razavi A, Wu H, Wang K, Freimuth F, Mokrousov Y, Stiles MD, Emori S, Hoffmann A, Åkerman J, Roy K, Wang JP, Yang SH, Garello K and Zhang W 2021 *IEEE Trans. Magn.* **57**, 1-39
[29] Yu G, Upadhyaya P, Fan Y, Alzate JG, Jiang W, Wong KL, Takei S, Bender SA, Chang LT and Jiang Y 2014 *Nat. Nanotechnol.* **9**, 548
[30] Cui B, Wu H, Li D, Razavi SA, Wu D, Wong KL, Chang M, Gao M, Zuo Y, Xi L and Wang KL 2019 *ACS Appl. Mater. Interfaces* **11**, 39369-39375
[31] Yu G, Chang L-T, Akyol M, Upadhyaya P, He C, Li X, Wong KL, Amiri PK and Wang KL 2014 *Appl. Phys. Lett.* **105**, 102411
[32] Zheng Z, Zhang Y, Lopez-Dominguez V, Sánchez-Tejerina L, Shi J, Feng X, Chen L, Wang Z, Zhang Z, Zhang K, Hong B, Xu Y, Zhang Y, Carpentieri M, Fert A, Finocchio G, Zhao W and Khalili Amiri P 2021 *Nat. Commun.* **12**, 4555
[33] Oh YW, Chris Baek SH, Kim YM, Lee HY, Lee KD, Yang CG, Park ES, Lee KS, Kim KW and Go G 2016 *Nat. Nanotechnol.* **11**, 878
[34] Fukami S, Zhang C, DuttaGupta S, Kurenkov A and Ohno H 2016 *Nat. Mater.* **15**, 535
[35] Cham TMJ, Dorrian RJ, Zhang XS, Dismukes AH, Chica DG, May AF, Roy X, Muller DA, Ralph DC and Luo YK 2024 *Adv. Mater.* **36**, 2305739
[36] Zhao B, Pandey L, Ali K, Wang E, Polley CM, Thiagarajan B, Makk P, Guimarães MHD and Dash SP 2025 *ACS Nano* **19**, 13817-13824
[37] Zhao B, Bainsla L, Ershadrad S, Zeng L, Ngaloy R, Svedlindh P, Olsson E, Sanyal B and Dash SP 2025 *Adv. Mater.* **37**, 2502822
[38] Zhao B, Bainsla L, Ershadrad S, Sumant PN, Ngaloy R, Rosen J, Sanyal B, Åkerman J

and Dash SP 2026 *Nano Lett.* **26**, 9631-9640
[39] Baek SC, Amin VP, Oh YW, Go G, Lee SJ, Lee GH, Kim KJ, Stiles MD, Park BG and Lee KJ 2018 *Nat. Mater.* **17**, 509
[40] Yun C, Guo H, Lin Z, Peng L, Liang Z, Meng M, Zhang B, Zhao Z, Wang L, Ma Y, Liu Y, Li W, Ning S, Hou Y, Yang J and Luo Z 2023 *Sci. Adv.* **9**, eadj3955
[41] Pu Y, Shi G, Yang Q, Yang D, Wang F, Zhang C and Yang H 2024 *Adv. Funct. Mater.* **34**, 2400143
[42] Yang Q, Han D, Zhao S, Kang J, Wang F, Lee SC, Lei J, Lee KJ, Park BG and Yang H 2024 *Nat. Commun.* **15**, 1814
[43] Lau Y-C, Betto D, Rode K, Coey JMD and Stamenov P 2016 *Nat. Nano.* **11**, 758-762
[44] Lai J-M, Hou R, Yan Z, Jin M, Wang F, Guo J, Zhang Y, Guo K, Zhao P, Bian B, Du Y, Lu W, Wang H, Yu Z, Shi G, Liu L, Yu G, Zhang L, Zhang D, Jiang Y and Xu X 2026 *ACS Nano* **20**, 16316-16324
[45] Pandey L, Zhao B, Tenzin K, Ngaloy R, Lamparská V, Bangar H, Ali A, Abdel-Hafiez M, Zhang G, Wu H, Chang H, Sjöström L, Rout P, Sławińska J and Dash SP 2025 *Nat. Commun.* **16**, 8722
[46] Zhang Y, Ren X, Liu R, Chen Z, Wu X, Pang J, Wang W, Lan G, Watanabe K, Taniguchi T, Shi Y, Yu G and Shao Q 2024 *Adv. Mater.* **36**, 2406464
[47] Li D, Liu X-Y, Ye X-G, Pan Z-C, Xu W-Z, Zhu P-F, Wang A-Q, Watanabe K, Taniguchi T and Liao Z-M 2024 *Phys. Rev. B* **110**, L100409
[48] Kajale SN, Nguyen T, Hung NT, Li M and Sarkar D 2024 *Sci. Adv.* **10**, eadk8669
[49] Yu Z, Yang L, Guo K, Zhao P, Hou R, Du Y, Lai JM, Quan Z, Wang F and Xu X 2025 *Adv. Funct. Mater.* **36**, 2505170
[50] Ali MN, Xiong J, Flynn S, Tao J, Gibson QD, Schoop LM, Liang T, Haldolaarachchige N, Hirschberger M, Ong NP and Cava RJ 2014 *Nature* **514**, 205-208
[51] Pletikosić I, Ali MN, Fedorov AV, Cava RJ and Valla T 2014 *Phys. Rev. Lett.* **113**, 216601
[52] Augustin J, Eyert V, Böker T, Frentrup W, Dwelk H, Janowitz C and Manzke R 2000 *Phys. Rev. B* **62**, 10812-10823
[53] Wang Y, Liu E, Liu H, Pan Y, Zhang L, Zeng J, Fu Y, Wang M, Xu K, Huang Z, Wang Z, Lu H-Z, Xing D, Wang B, Wan X and Miao F 2016 *Nat. Commun.* **7**, 13142
[54] MacNeill D, Stiehl GM, Guimaraes MHD, Buhrman RA, Park J and Ralph DC 2017 *Nat. Phys.* **13**, 300-305
[55] Kao IH, Muzzio R, Zhang H, Zhu M, Gobbo J, Yuan S, Weber D, Rao R, Li J, Edgar JH, Goldberger JE, Yan J, Mandrus DG, Hwang J, Cheng R, Katoch J and Singh S 2022 *Nat. Mater.* **21**, 1029-1034
[56] Shin I, Cho WJ, An E-S, Park S, Jeong H-W, Jang S, Baek WJ, Park SY, Yang D-H, Seo JH, Kim G-Y, Ali MN, Choi S-Y, Lee H-W, Kim JS, Kim SD and Lee G-H 2022 *Adv. Mater.* **34**, 2101730
[57] Wei L, Yin X, Liu P, Zhang P, Niu W, Liu P, Yang J, Peng J, Huang F and Liu R 2023 *Appl. Phys. Lett.* **123**, 252404
[58] Sharma PR, Jang B, Zhang G, Jin W, Chang H and Hong J 2025 *Appl. Surf. Sci. Adv.* **29**, 100847
[59] Liu Y, Shi G, Kumar D, Kim T, Shi S, Yang D, Zhang J, Zhang C, Wang F, Yang S, Pu Y,

Yu P, Cai K and Yang H 2023 *Nat. Electron.* **6**, 732-738
[60] Zhang Y, Xu H, Jia K, Lan G, Huang Z, He B, He C, Shao Q, Wang Y and Zhao M 2023 *Sci. Adv.* **9**, eadg9819
[61] Bainsla L, Zhao B, Behera N, Hoque AM, Sjöström L, Martinelli A, Abdel-Hafiez M, Åkerman J and Dash SP 2024 *Nat. Commun.* **15**, 4649
[62] Yang W, Wang X, Liu J, Zhou D, Lin X, Zhang K, Damas H, Wang X, Lu X, Yang H, Mangin S, Petit-Watelot S, Hehn M, Albert F, Rojas Sánchez JC and Zhao W 2025 *arXiv* 2504.05280v05281
[63] Fei Z, Huang B, Malinowski P, Wang W, Song T, Sanchez J, Yao W, Xiao D, Zhu X, May AF, Wu W, Cobden DH, Chu J-H and Xu X 2018 *Nat. Mater.* **17**, 778-782
[64] Tan C, Lee J, Jung S-G, Park T, Albarakati S, Partridge J, Field MR, McCulloch DG, Wang L and Lee C 2018 *Nat. Commun.* **9**, 1554
[65] Liu B, Liu S, Yang L, Chen Z, Zhang E, Li Z, Wu J, Ruan X, Xiu F, Liu W, He L, Zhang R and Xu Y 2020 *Phys. Rev. Lett.* **125**, 267205
[66] Zhang G, Guo F, Wu H, Wen X, Yang L, Jin W, Zhang W and Chang H 2022 *Nat. Commun.* **13**, 5067
[67] Lee JE, Yan S, Oh S, Hwang J, Denlinger JD, Hwang C, Lei H, Mo SK, Park SY and Ryu H 2023 *Nano Lett.* **23**, 11526-11532
[68] Ruiz AM, Esteras DL, López-Alcalá D and Baldoví JJ 2024 *Nano Lett.* **24**, 7886-7894
[69] Wang M, Lei B, Zhu K, Deng Y, Tian M, Xiang Z, Wu T and Chen X 2024 *npj 2D Mater. Appl.* **8**, 22
[70] Jia ZY, Zhao MF, Chen Q, Tian YX, Liu LX, Zhang F, Zhang DL, Ji Y, Camargo B, Ye K, Sun R, Wang ZC and Jiang Y 2025 *ACS Nano* **19**, 9452-9483
[71] Tang W, Liu H, Li Z, Pan A and Zeng Y-J 2021 *Adv. Sci.* **8**, 2100847
[72] Lin X and Zhu L 2023 *Mater. Today Electron.* **4**, 100037
[73] Marfoua B and Hong J 2024 *Mater. Today Phys.* **42**, 101378
[74] Jia Z, Zhao M, Chen Q, Tian Y, Liu L, Zhang F, Zhang D, Ji Y, Camargo B, Ye K, Sun R, Wang Z and Jiang Y 2025 *ACS Nano* **19**, 9452-9483
[75] Wang L, Xiong J, Cheng B, Dai Y, Wang F, Pan C, Cao T, Liu X, Wang P, Chen M, Yan S, Liu Z, Xiao J, Xu X, Wang Z, Shi Y, Cheong S-W, Zhang H, Liang S-J and Miao F 2022 *Sci. Adv.* **8**, eabq6833
[76] Pan Z-C, Li D, Ye X-G, Chen Z, Chen Z-H, Wang A-Q, Tian M, Yao G, Liu K and Liao Z-M 2023 *Sci. Bull.* **68**, 2743-2749
[77] Huang P, Liu X, Xin Y, Gu Y, Lee A, Zhang Y, Xu Z, Chen P, Zhang Y, Deng W, Yu G, Wu D, Liu Z, Yao Q, Yang Y, Zhu Z and Kou X 2024 *ACS Nano* **18**, 29469-29478
[78] Yang Q, Zhao S, Wang F, Pu Y, Li Z, Chen X, Lei J and Yang H 2025 *Adv. Funct. Mater.* **35**, 2507988
[79] Gao F, Wang Z, Zhao R, Li J, Song X, Yu P, Sun Y, Xie W, Wei G, Yao Y, Zou J, Zhang J, Xing S, Mantovan R, Guo Z, Jaouen N, Zhao W and Nie T 2026 *Nat. Commun.* **17**, 3826
[80] Qian Chen WLSLWLJCYZJWRLBZ and Zhongming Z 2021 *Chin. Phys. B* **30**, 97506-097506
[81] Liu X, Wu D, Liao L, Chen P, Zhang Y, Xue F, Yao Q, Song C, Wang KL and Kou X 2021 *Appl. Phys. Lett.* **118**, 112406
[82] Han J, Richardella A, Siddiqui SA, Finley J, Samarth N and Liu L 2017 *Phys. Rev. Lett.*

119, 077702
[83] Chen X, Liu Y, Yang G, Shi H, Hu C, Li M and Zeng H 2018 *Nat. Commun.* **9**, 2569
[84] Dc M, Grassi R, Chen J-Y, Jamali M, Reifsnyder Hickey D, Zhang D, Zhao Z, Li H, Quarterman P, Lv Y, Li M, Manchon A, Mkhoyan KA, Low T and Wang J-P 2018 *Nat. Mater.* **17**, 800-807
[85] Alghamdi M, Lohmann M, Li J, Jothi PR, Shao Q, Aldosary M, Su T, Fokwa BPT and Shi J 2019 *Nano Lett.* **19**, 4400-4405
[86] Wang X, Tang J, Xia XX, He CL, Zhang JW, Liu YZ, Wan CH, Fang C, Guo CY, Yang WL, Guang Y, Zhang XM, Xu HJ, Wei JW, Liao MZ, Lu XB, Feng JF, Li XX, Peng Y, Wei HX, Yang R, Shi DX, Zhang X, Han Z, Zhang ZD, Zhang GY, Yu G and Han XF 2019 *Sci. Adv.* **5**, eaaw8904
[87] Gupta V, Cham TM, Stiehl GM, Bose A, Mittelstaedt JA, Kang K, Jiang S, Mak KF, Shan J, Buhrman RA and Ralph DC 2020 *Nano Lett.* **20**, 7482-7488
[88] Wang M, Guo Q, Xu X, Zhang Z, Ren Z, Zhu L, Meng K, Chen J, Wu Y, Miao J and Jiang Y 2020 *Adv. Electron. Mater.* **6**, 2000229
[89] Tang M, Shen K, Xu S, Yang H, Hu S, Lu W, Li C, Li M, Yuan Z, Pennycook SJ, Xia K, Manchon A, Zhou S and Qiu X 2020 *Adv. Mater.* **32**, e2002607
[90] Deng Y, Yu Y, Song Y, Zhang J, Wang NZ, Sun Z, Yi Y, Wu YZ, Wu S, Zhu J, Wang J, Chen XH and Zhang Y 2018 *Nature* **563**, 94-99
[91] Zhu J-X, Janoschek M, Chaves DS, Cezar JC, Durakiewicz T, Ronning F, Sassa Y, Mansson M, Scott BL, Wakeham N, Bauer ED and Thompson JD 2016 *Phy. Rev. B* **93**, 144404
[92] Zhu K, Wang M, Deng Y, Tian M, Lei B and Chen X 2024 *Phys. Rev. B* **109**, 104402
[93] Kajale SN, Nguyen T, Chao CA, Bono DC, Boonkird A, Li M and Sarkar D 2024 *Nat. Commun.* **15**, 1485
[94] Mogi M, Yasuda K, Fujimura R, Yoshimi R, Ogawa N, Tsukazaki A, Kawamura M, Takahashi KS, Kawasaki M and Tokura Y 2021 *Nat. Commun.* **12**, 1404
[95] Tai L, He H, Chong SK, Zhang H, Huang H, Qiu G, Ren Y, Li Y, Yang H-Y, Yang T-H, Dong X, Dai B, Qu T, Shu Q, Pan Q, Zhang P, Xue F, Li J, Davydov AV and Wang KL 2024 *Adv. Mater.* **36**, 2406772
[96] Choi GS, Park S, An E-S, Bae J, Shin I, Kang BT, Won CJ, Cheong S-W, Lee H-W, Lee G-H, Cho WJ and Kim JS 2024 *Adv. Sci.* **11**, 2400893
[97] Qiu X, Deorani P, Narayanapillai K, Lee K-S, Lee K-J, Lee H-W and Yang H 2014 *Sci. Rep.* **4**, 4491
[98] Xu H, Wei J, Zhou H, Feng J, Xu T, Du H, He C, Huang Y, Zhang J and Liu Y 2020 *Adv. Mater.* **32**, e2000513
[99] Li W, Zhu W, Zhang G, Wu H, Zhu S, Li R, Zhang E, Zhang X, Deng Y, Zhang J, Zhao L, Chang H and Wang K 2023 *Adv. Mater.* **35**, 2303688
[100] Wang Y, Zhu D, Wu Y, Yang Y, Yu J, Ramaswamy R, Mishra R, Shi S, Elyasi M, Teo K-L, Wu Y and Yang H 2017 *Nat. Commun.* **8**, 1364
[101] Wang H, Wu H, Zhang J, Liu Y, Chen D, Pandey C, Yin J, Wei D, Lei N, Shi S, Lu H, Li P, Fert A, Wang KL, Nie T and Zhao W 2023 *Nat. Commun.* **14**, 5173
[102] Zhu L and Ralph DC 2023 *Nat. Commun.* **14**, 1778
[103] Jiang M, Asahara H, Sato S, Ohya S and Tanaka M 2020 *Nat. Electron.* **3**, 751-756

[104] Xu H, Wei J, Zhou H, Feng J, Xu T, Du H, He C, Huang Y, Zhang J, Liu Y, Wu HC, Guo C, Wang X, Guang Y, Wei H, Peng Y, Jiang W, Yu G and Han X 2020 *Adv. Mater.* **32**, 2000513
[105] Deng Y, Wang M, Xiang Z, Zhu K, Hu T, Lu L, Wang Y, Ma Y, Lei B and Chen X 2024 *Nano Lett.* **24**, 9302-9310
[106] Guillet T, Galceran R, Sierra JF, Belarre FJ, Ballesteros B, Costache MV, Dosenovic D, Okuno H, Marty A, Jamet M, Bonell F and Valenzuela SO 2024 *Nano Lett.* **24**, 822-828
[107] Xu T, Xu Z, Dong Y, Cheng Y, Wang L, Feng H, Bai H, Xu K, Shu X, Yu P, Zhou H-A, Liu E, He S, Xi C, Yu G, Qiu X, Kim SK, Zhu J, Zhu Z and Jiang W 2025 *Phys. Rev. Lett.* **135**, 126703
[108] Kang M-G, Lee S and Park B-G 2025 *npj Spintronics* **3**, 8
[109] Yang M, Sun L, Zeng Y, Cheng J, He K, Yang X, Wang Z, Yu L, Niu H, Ji T, Chen G, Miao B, Wang X and Ding H 2024 *Nat. Commun.* **15**, 3201
[110] Chen S, Tang Z, Fang M, Sun R, Zhang X, Xiao L, Mohajerani SS, Liu N, Zhang Y, Sarkar AS, Sun D, Strauf S and Yang EH 2025 *Adv. Funct. Mater.* **35**, 2418647
[111] Han F, Zhang J, Yang F, Li B, He Y, Li G, Chen Y, Jiang Q, Huang Y and Zhang H 2024 *Nat. Commun.* **15**, 7299
[112] Kong WJ, Wan CH, Wang X, Tao BS, Huang L, Fang C, Guo CY, Guang Y, Irfan M and Han XF 2019 *Nat. Commun.* **10**, 233
[113] Wang F, Shi G, Kim K-W, Park H-J, Jang JG, Tan HR, Lin M, Liu Y, Kim T, Yang D, Zhao S, Lee K, Yang S, Soumyanarayanan A, Lee K-J and Yang H 2024 *Nat. Mater.* **23**, 768-774
[114] Wang F, Shi G, Yang D, Tan HR, Zhang C, Lei J, Pu Y, Yang S, Soumyanarayanan A and Elyasi M 2024 *Nat. Nanotechnol.* **19**, 1478
[115] Wang X, Wu H, Qiu R, Huang X, Zhang J, Long J, Yao Y, Zhao Y, Zhu Z and Wang J 2023 *Cell Rep. Phys. Sci.* **4**, 101468
[116] Liang S, Shi S, Hsu CH, Cai K, Wang Y, He P, Wu Y, Pereira VM and Yang H 2020 *Adv. Mater.* **32**, e2002799
[117] Liu L, Zhou C, Shu X, Li C, Zhao T, Lin W, Deng J, Xie Q, Chen S, Zhou J, Guo R, Wang H, Yu J, Shi S, Yang P, Pennycook S, Manchon A and Chen J 2021 *Nat. Nano.* **16**, 277-282
[118] Dc M, Shao D-F, Hou VDH, Vailionis A, Quarterman P, Habiboglu A, Venuti MB, Xue F, Huang Y-L, Lee C-M, Miura M, Kirby B, Bi C, Li X, Deng Y, Lin S-J, Tsai W, Eley S, Wang W-G, Borchers JA, Tsymbal EY and Wang SX 2023 *Nat. Mater.* **22**, 591-598
[119] Shi G, Wang F, Liu Y, Li Z, Tan HR, Yang D, Soumyanarayanan A and Yang H 2024 *Nano Lett.* **24**, 7302
[120] Shi S, Liang S, Zhu Z, Cai K, Pollard SD, Wang Y, Wang J, Wang Q, He P, Yu J, Eda G, Liang G and Yang H 2019 *Nat. Nanotechnol.* **14**, 945-949
[121] Zhang K-X, Cheon S, Lee S, Choi J, Keum J, Kim H, An Y, Cho W, Son S, Cui J, Park P, Jo Y, Kim JS, Lee H-W and Park J-G 2026 *Nat. Commun.* **17**, 8620
[122] Shi S, Wang X, Zhao Y and Zhao W 2023 *Mater. Today Electron.* **6**, 100060
[123] Tian M, Zhu Y, Jalali M, Jiang W, Liang J, Huang Z, Chen Q, Zeng Z and Zhai Y 2021 *Front. Nanotechnol.* **3**, 732916
[124] Liu X, Huang P, Xia Y, Gao L, Liao L, Cui B, Backes D, van der Laan G, Hesjedal T, Ji

Y, Chen P, Zhang Y, Wu F, Wang M, Zhang J, Yu G, Song C, Chen Y, Liu Z, Yang Y, Peng Y, Li G, Yao Q and Kou X 2023 *Adv. Funct. Mater.* **33**, 2304454